Supporting Information

Crystalline Metal Organic Frameworks Built with Barrierless Molecular Rotors – A Promising Platform for Rotary Arrays and Ultrafast Molecular Machines

Cortnie S. Vogelsberg,[a] Fernando J. Uribe-Romo,[b] Andrew Lipton,[C] Song Yang,[a] K.N. Houk,[a] Stuart Brown,[d] Miguel A. Garcia-Garibay[a]

a) Department of Chemistry and Biochemistry, University of California, Los Angeles, CA 90095; b) Department of Chemistry, University of Central Florida, Orlando, FL 32816; c) Pacific Northwest National Laboratory, High Field Magnetic Resonance Facility, Richland, WA 99352; d) Department of Physics and Astronomy, University of California, Los Angeles, CA 90095;

Page

S4 **Stepwise linear synthesis of BODCA ligand and BODCA MOF**

S4 **Scheme SI-1.** Stepwise linear synthesis of the BODCA ligand, shown with modifications to install deuterons on the bicyclic core with the average statistical ^{2}H content indicated.

S4 **Solvents used**

S5 **Dimethyl 2,5-dioxobicyclo[2.2.2]octane-1,4-dicarboxylate (1)**

S5 **Dimethyl 2,5-bicyclo[2.2.2]octane-2,5-diethyleneketal-1,4-dicarboxylate (2)**

S6 **Bicyclo[2.2.2]octane-2,5-diethyleneketal-1,4-dimethanol (3)**

S6 **1,4-bis(hydroxymethyl)bicyclo[2.2.2]octane-2,5-dione (4)**

S7 **Bicyclo[2.2.2]octane-H/D-1,4-diyldimethanol (5**-d)

S9 **Figure SI-1.** Statistical substitution in diol **5**-*d* (and similarly, for diacid **6**-*d*).

S10 **Figure SI-2.** For the quaternary bridgehead carbon of diol **5**-*d*, to which no deuterons may be attached, striking consequences are observed due to ^{2}H substitution arising from chemical shift effects,

S10 **Bicyclo[2.2.2]octane-H/D-1,4-dicarboxylic acid (BODCA) (6**-*d).*

S11 **Scheme SI-2.** One-pot synthesis of BODCA MOF, where red represents the dynamic rotator moieties and blue represents the static carboxylate and ligand clusters relative to the rotator.

S12 **Bicyclo[2.2.2]octane-H/D-1,4-dicarboxlate metal-organic framework (BODCA MOF).**

S14 **Spectral Data**

S14 **Figure SI-3.** ATR FT-IR spectrum of **2**

S15 **Figure SI-4.** ^{1}H NMR (CDCl$_3$, 300 MHz) spectrum of **2**.

S16 **Figure SI-5.** ^{13}C NMR (CDCl$_3$, 75 MHz) spectrum of **2**.

S17 **Figure SI-6.** ATR FT-IR spectrum of **5**-*d*.

S18 **Figure SI-7** ^{1}H NMR (CDCl$_3$, 500 MHz) spectrum of **5**-*d*.

S19 **Figure SI-8.** ^{13}C NMR (CDCl$_3$, 125 MHz) spectrum of **5**-*d* (full spectrum).

S20 **Figure SI-9.** ^{13}C NMR (CDCl$_3$, 125 MHz) spectrum of **5**-*d* (zoom in of C—^{2}H coupling and ^{2}H isotope effects on the ^{13}C chemical shift).

S21 **Figure SI-10.** ^{1}H NMR (CDCl$_3$, 600 MHz) spectrum of **5**-*d*.

S22 **Figure SI-11.** ^{13}C NMR (CDCl$_3$, 125 MHz) spectrum of **5**-*d* (full spectrum).

S23 **Figure SI-12.** ^{13}C NMR (CDCl$_3$, 150 MHz) spectrum of **5**-*d* (zoom in of C—^{2}H coupling and ^{2}H isotope effects on the ^{13}C chemical shift).

S24 **Figure SI-13.** ATR FT-IR spectrum of **6**-*d*.

S25 **Figure SI-14.** ^{1}H NMR (CD$_3$OD, 500 MHz) spectrum of **6**-*d*

S26 **Figure SI-15.** ^{13}C NMR (CD$_3$OD, 125 MHz) spectrum of **6**-*d*

S27 **Figure SI-16** ^{13}C NMR (CD$_3$OD, 125 MHz) spectrum of **6**-*d.*

S28 **Figure SI-17.** ATR FT-IR spectrum of **6**.

S29 **Figure SI-18.** ^{1}H NMR (SO(CD$_3$)$_2$, 300 MHz) spectrum of **6**.

S30 **Figure SI-19.** ^{13}C NMR (SO(CD$_3$)$_2$, 75 MHz) spectrum of **6**.

S31 **Figure SI-20.** Liquid introduction field desorption ionization (LIFDI) mass spectrum of **5**-*d*. (a) Zoom out. (b) Zoom in to molecular ion, with peaks corresponsing to varying degrees of deuteron substitution.

S32 **Figure SI-21.** Liquid introduction field desorption ionization (LIFDI) mass spectrum of **6**-*d*. (a) Zoom out. (b) Zoom in to molecular ion, with peaks corresponsing to varying degrees of deuteron substitution.

S33 **Figure SI-22.** Activated BODCA MOF ATR FT-IR spectrum.

S34 **Figure SI-23.** Freshly activated BODCA MOF thermogravimetric analysis. (2.955 mg of sample, ramp = 25.00 °C to 505.00 °C at rate 5.00 °C min^{-1}).

S35 **Figure SI-24.** Activated BODCA MOF ^{13}C CP/MAS NMR spectrum, acquired by sandwiching between layers of anhydrous magnesium sulfate desiccant in the 4 mm rotor to prevent decomposition from ambient moisture. (MAS = 10 kHz, contact time = 4.4 microseconds, recycle delay = 20 s).

S36 **PXRD Structural analysis**

S36 **Figure SI-25.** Experimental (blue ticks) and refined (red line) PXRD patterns of BODCA MOF after Rietveld refinement compared to the calculated pattern (black line) of the crystal model. The position of the Bragg reflections and the refinement difference plot are indicated as purple ticks and green line, respectively.

S37 **Unit Cell Determination**

S37 **Pawley Refinements**

S37 **Electron Density Calculation**

S38 **Figure SI-26**. Example of a reconstructed electron density map obtained from *SUPERFLIP* (viewed along the 100 direction).

S38 **Rietveld Refinements**

S38 **Crystal Structure Modeling**

S40 **Table SI-1.** Crystallographic information from Rietveld Refinement.

S42 **Table SI-2.** Atomic Coordinates

S42 **Adsorption Isotherm data of BODCA-d MOF**

S43 **Figure SI-27**. The dinitrogen adsorption isotherm (77 K) displays a sharp uptake with a single adsorption step at $p/p_o > 0.01$ followed by saturation, indicating a microporous material. It can be also described as a Type II isotherm under the IUPAC classification system. (a) Linear pressure scale. (b) Log pressure scale. In the figure, the adsorption branch is represented by filled symbols and the desorption branch by open symbols, indicating the reversibility of the adsorption with no evident hysteresis.

S44 **Figure SI-28.** Application of the Brunauer-Emmett-Teller (BET) model over $0.005 > p/p_o > 0.05$, according to the recommendation by Snurr *et al.* resulted in a BET surface area of $S_{BET} = 2150$ $m^2 g^{-1}$.

S44 **Figure SI-29.** The total pore volume was determined from the Dubinin-Raduschevich (DR) model over the $0.13 > p/p_o > 0.35$ range, obtaining a $V_{p,DR} = 0.8630$ $cm^3 g^{-1}$.

S45 **Solid State NMR Spectroscopy**

S45 **^{13}C CPMAS**

S45 **^{1}H Spin-Lattice Relaxation**

S48 **Figure SI-30.** (a) Kubo-Tomita fit (black lines) to the ^{1}H T_1 relaxation data of the natural abundance BODCA MOF from T = 2.3 - 80 K, plotted with a semi-log scale for T_1^{-1} VS 1/T, where red corresponds to data collected at a Larmor frequency v_L= 29.49 MHz and yellow corresponds to v_L = 13.87 MHz. The high temperature data from both high and low field experiments can be fit well to the Kubo-Tomita fit, revealing an activation energy of only *ca.* 0.185 kcal mol^{-1} and a pre-exponential factor of 4.7×10^{10} Hz for both fits. (b) A zoom in of the data shows that the ^{1}H T_1 minimum occurs approximately 2.2 K lower at the lower field, in good agreement with the Kubo-Tomita fit for the same thermally activated process occurring at the two different Larmor frequencies.

S49 **Figure SI-31.** ^{1}H spin-lattice relaxation of the natural abundance BODCA MOF at 29.49 MHz, T = 2.3 K, fit to a single exponential.

S49 **Figure SI-32.** Fully recovered spectrum of natural abundance BODCA MOF, T = 2.3 K, of at a Larmor frequency of 29.49 MHz.

S50 **Figure SI-33.** Stack plot of ^{1}H T_1 saturation recovery spectra according to the delay time tau (s) of the natural abundance BODCA MOF at 2.3 K and at a Larmor frequency of 29.49 MHz (*x*-axis in Hz).

S51 **Figure SI-34.** ^{1}H spin-lattice relaxation of the natural abundance BODCA MOF at 29.49 MHz, T = 49 K, fit to a single exponential.

S51 **^{2}H Wideline Spectra and Zeeman Spin-Lattice Relaxation**

S52 **Figure SI-35.** A saturation recovery sequence was employed to acquire periodically the ^{2}H spin-lattice relaxation times (T_1) as a function of temperature to enable selection of an appropriate recycle delay in the solid-echo experiments, shown with data corresponding to cooling and warming ramps in yellow and red, respectively. A minimum in relaxation time occurs at T ~ 21 K at a ^{2}H Larmor frequency of 76.78 MHz. This is consistent with the ^{1}H T_1 data, which shows a minimum in spin-lattice relaxation time at 18.2 K at a slightly lower Larmor frequency of 29.49 MHz, suggesting that the same motional process is being probed in each of the different experiments. At ~ 51 K and below, the ^{2}H spin-lattice relaxation deviates from single exponential behavior. This is consistent with the idea that at low temperatures, additional spin relaxation processes besides dynamical averaging may occur.

S53 **Computational Details**

STEPWISE LINEAER SYNTHESIS OF BODCA LIGAND AND BODCA MOF

Scheme SI-1. Stepwise linear synthesis of the BODCA ligand, shown with modifications to install deuterons on the bicyclic core, with the average statistical ^{2}H content shown in blue.

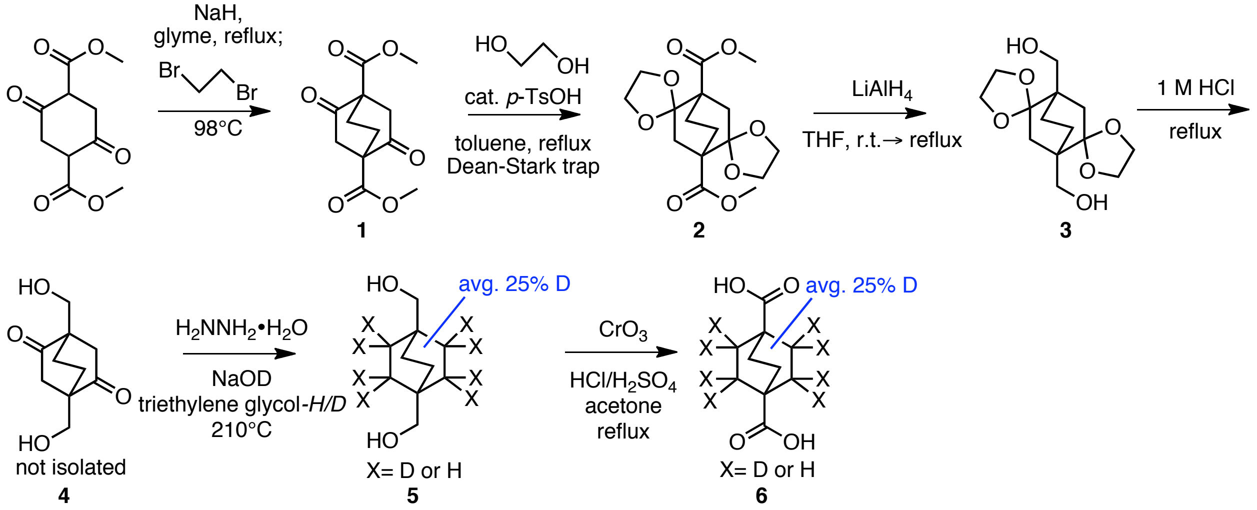

Solvents. With the exception of glyme, triethylene glycol-*H/*D, dimethyl formamide, tetrahydrofuran, and dichloromethane (*vide infra*), all solvents were used as purchased. Glyme was distilled from CaH_2 immediately before use. Triethylene glycol-*H/D*, or $XO(CH_2CH_2O)_2CH_2CH_2OX$ where X is deuterium, was prepared by mixing 30 mL of triethylene glycol-*H* (99%, Sigma-Aldrich) with 30 mL of deuterium oxide (D 99.9%, Cambridge Isotope Laboratories, Inc.) overnight, followed by removal of all water isotopologues *via* vacuum distillation—this process was repeated three times to achieve hydrogen/deuterium exchange of the hydroxy group. *N*,*N*-dimethylformamide (DMF) was dried for 24 hours over activated 3Å molecular sieves. Tetrahydrofuran (THF) was dried over Na in the presence of benzophenone indicator in a solvent distilling head under inert atmosphere. For use in the MOF synthesis only, the dichloromethane was dried over CaH_2 in a solvent distilling head under inert atmosphere.

Dimethyl 2,5-dioxobicyclo[2.2.2]octane-1,4-dicarboxylate (1).[1] Diester **1** was prepared according to a known literature procedure. A 2 L three-necked flask fitted with a stir bar and a water condenser was flame dried and cooled under an Ar(*g*) atmosphere. To this was added 20 g (0.5 mol) of NaH 60% dispersion in mineral oil, which was subsequently suspended in 500 mL glyme. Next, 64.0 g (0.28 mol) of dimethyl 2,5-dioxocyclohexane-1,4-dicarboxylate was added slowly and in small portions. After the addition was complete, the solution was refluxed for three hours until the color changed from an off white to a vibrant purple. The glyme was then removed *via* distillation to obtain a thick purple paste. 500 mL of 1,2-dibromoethane previously dried *via* distillation from CaH_2 was added to the purple paste, and the solution was refluxed at 95 ºC until the solution color changed to an off white. The excess 1,2-dibromoethane was removed *via* vacuum distillation. The solid was dissolved in dichloromethane and washed with 1% NaOH, water, and finally brine. The organic portion was separated, dried over anhydrous $MgSO_4$ and then filtered. The dichloromethane was subsequently removed *via* rotary evaporation to yield an off white solid. The solid was then recrystallized from ethanol to obtain 43.1 g (60%) isolated yield of **1**. The physical properties and spectroscopic data for **1** were consistent with those reported in the literature.[1]

Dimethyl 2,5-bicyclo[2.2.2]octane-2,5-diethyleneketal-1,4-dicarboxylate (2). Bisketal **2** was prepared identically to known literature procedure for the diethyl 2,5-bicyclo[2.2.2]octane-2,5-diethyleneketal-1,4-dicarboxylate derivative. 12.7 g (50 mmol) of **1**, 460 mL of benzene, 11.1 mL of ethylene glycol, and 0.5 g *p*-toluene sulfonic acid monohydrate were combined in a 1 L one-necked round bottom flask equipped with a stir bar. The setup was fitted with a Dean-Stark trap and a water condenser, and the mixture was refluxed for 60 hours. The reaction mixture was quenched with 1 M KOH solution. The resulting organic layer was separated from the aqueous layer and dried over anhydrous $MgSO_4$. The drying agent was subsequently removed by filtration, and the benzene was removed by rotary evaporation to yield 13.1 g of a pale yellow oil of spectroscopic purity in 77% yield. The spectroscopic data for dimethyl ester **2** were similar with those reported in the literature for the diethyl ester analogue (See Chapter 2, section **2.4.1.3**). ^{1}H NMR (300 MHz, $CDCl_3$): *δ* (ppm) 3.94 (m, 6H), 3.73 (m, 2H), 3.67 (s, 6H), 2.45 (dd, *J* = 14.4 Hz, *J* = 2.7 Hz, 2H), 2.32 (m, 2H), 1.99 (d, *J* = 14.4 Hz, 2H), 1.70 (m, 2H). ^{13}C NMR (75 MHz, $CDCl_3$): *δ* (ppm) 173.22, 110.20, 65.11, 64.94, 52.19, 49.07, 41.85, 24.16. ATR FT-IR (cm^{-1}): 2984.12, 2948.41, 2892.85, 1728.41, 1437.00,127048, 1074.22.

Bicyclo[2.2.2]octane-2,5-diethyleneketal-1,4-dimethanol (3).[1, 2] Diol **3** was prepared identically to known literature procedure based on the diethyl 2,5-bicyclo[2.2.2]octane-2,5-diethyleneketal-1,4-dicarboxylate derivative. A 500 mL three-necked round bottom flask fitted with a stir bar, water condenser, and addition funnel were flame dried and cooled under an Ar(*g*) atmosphere. 7.0 g (175 mmol) of 95% lithium aluminum hydride (LAH) was added to the three-necked flask and dispersed in 130 mL of THF. Subsequently, 13.1 g (38 mmol) of diketal diester **2** was dissolved in 125 mL THF in the addition funnel with the aid of a heat gun. The solution of **2** was then added drop wise to the LAH suspension at room temperature over the course of one hour, and then refluxed for an additional 2.5 hours. The solution was then cooled to room temperature, and water was added drop wise to quench the reaction until no grey color was observed. The organic portion was then extracted with diethyl ether (3 × 500 mL). The diethyl ether was removed *via* rotary evaporation resulting in 10.3 g (95%) isolated yield of a clear oil. The spectroscopic data for **2** were consistent with those reported in the literature.[2]

1,4-bis(hydroxymethyl)bicyclo[2.2.2]octane-2,5-dione (4).[2] Dione **4** was prepared according to a known literature procedure. 10.3 g (36 mmol) of **3** was dissolved in 500 mL of 1 M HCl (*aq.*) in a 1 L round bottom flask fitted with a water condenser and stir bar, and the solution was refluxed for three hours. The mixture was then cooled to room temperature and neutralized to a pH of 7 using 0.1 M KOH. The water was removed *via* rotary evaporation to yield a sticky off white salt. The salt was suspended in 500 mL was acetone. The white solid was then separated from the organic portion. The acetone was removed by rotary evaporation to yield an oil composed of a ~1:2 mixture of bicyclo[2.2.2]octane-2,5-diketo-1,4-dimethanol (**4**):ethylene glycol. The spectroscopic data of the mixture was consistent with those reported in the literature, and was used in the next step without further purification.[2]

Bicyclo[2.2.2]octane-*H/D*-1,4-diyldimethanol (5-*d*). Bicyclo[2.2.2]octane-*H/D*-1,4-dimethanol **5** was prepared using a modified literature procedure based on the Huang-Minglon modified Wolff-Kishner reduction of **4**. 2.5 g of an oil composed of a ~1:2 mixture of bicyclo[2.2.2]octane-2,5-diketo-1,4-dimethanol (**4**):ethylene glycol ($MW_{\sim 1:2\ \text{mixture}}$ = 322.16 g mol^{-1}) from the previous step (constituting approximately 7.8 mmol of bicyclo[2.2.2]octane-2,5-diketo-1,4-dimethanol) was added to a 50 mL 14/20 round bottom flask equipped with a stir bar. To this oil was added 4 *eq*. of hydrazine monohydrate (31.2 mmol) and 5.7 *eq*. of NaOD (46.6 mmol) in triethylene glycol-*H/D*, prepared by carefully adding 1.0 g of Na in very small portions to 1.5 mL of deuterium oxide, subsequently adding 18 mL triethylene glycol-*H/D*, and removing excess water isotopologues *via* vacuum distillation. The setup was fitted with a water condenser, and the reaction mixture was heated at ~210 ºC for 36 hours. The solution was then cooled to room temperature and acidified to a pH of 2 using 1 M HCl (aq.). The organic portion was extracted with chloroform (3 × 150 mL). The resulting organic portions were combined and washed with water and then brine, and finally dried over anhydrous $MgSO_4$. The dried organic portion was filtered and rotoevaporated to dryness. Recrystallization from chloroform resulted in 332 mg of a white, crystalline solid in an isolated yield of ~24%. Integration of the bridging methylenes *versus* the methanol methylenes from the ^1H NMR spectrum of **5**-*d* in $CDCl_3$ acquired on a Bruker AV500 NMR spectrometer showed that there were, on average, three deuterons instilled on the bicyclo[2.2.2]octane core. ^1H NMR (500 MHz, $CDCl_3$) δ (ppm): 3.26 (s, 4H), 1.41 (s), 1.40 (s), 1.38 (s). ^{1}H NMR (600 MHz, $CDCl_3$) δ (ppm): 3.26 (s, 4H), 1.41 (s), 1.40 (s), 1.38 (s). ^{13}C NMR (125 MHz, $CDCl_3$) δ (ppm): 71.60, 33.72, 33.64, 33.55, 33.46, 33.82, 27.80, 27.77, 27.75, 27.69, 27.67, 27.25 (p, 19.5 Hz, split due to $^{1}\Delta$, $^{2}\Delta$, $^{3}\Delta$, and $^{4}\Delta$ ^{2}H chemical shift isotope effects of *ca*. 3.2 Hz). ^{13}C NMR (150 MHz, $CDCl_3$) δ (ppm): 71.61, 33.75, 33.74, 33.72, 33.65, 33.64, 33.57, 33.56, 33.49, 33.48, 27.83, 27.80, 27.77, 27.72, 27.69, 27.27 (p, 19.5 Hz, split due to $^{1}\Delta$, $^{2}\Delta$, $^{3}\Delta$, and $^{4}\Delta$ ^{2}H chemical shift isotope effects of *ca*. 4.1 Hz). ATR FT-IR (cm^{-1}): 3305.55, 2921.12, 2913.57, 2903.18, 2855.96, 1467.59, 1451.87, 1444.02, 1370.66, 1020.70. .MP: 108-109 ºC (Lit. 107-108 for natural abundance). Liquid Introduction Field Desorption Ionization Mass Spectrometry (*m*/*z*): M^{+}= 170 (D_0), 171 (D_1), 172 (D_2), 173 (D_3), 174 (D_4), 175 (D_5), 176 (D_6), 177 (D_7). The natural abundance diol **5** was prepared according to a known literature procedure, using a similar Huang-Minglon modified Wolff-Kishner reduction of **4** used to generate **5**-*d*. The spectroscopic data of the mixture was consistent with those reported in the literature, and was used in the next step without further purification.

As expected, the ^{1}H and ^{13}C solution NMR spectra of diol **5**-*d* **(**and diacid **6**-*d*, see below) display chemical shifts and coupling from isotope effects due to the various substitution patterns of the deuterons (Figures SI-1 and SI-2) with respect to the NMR-active ^{1}H and ^{13}C nuclei (for NMR and FT-IR spectra, see Figs. A.5.5. – A.5.14.). The NMR chemical shift effects scale with applied magnetic field strength (*e.g.*, an applied field strength of 14.1 T results in *ca.* 16% larger values, *versus* an applied field strength of than 11.7 T). Similar $^{1}\Delta$, $^{2}\Delta$, $^{3}\Delta$, and $^{4}\Delta$ deuterium isotope effects on ^{13}C chemical shifts have previously been observed in a related rigid, bicyclic system (protoadamantane) and the effects are additive.[3] Therefore, the effect on the chemical shift due to the presence of deuterium on the methylene bridge carbons may be mathematically represented by the expression $\Delta\delta_{\mathrm{methylene}} = \sum_{i=0}^{2} {}^{1}\Delta + \sum_{j=0}^{2} {}^{2}\Delta + \sum_{k=0}^{2} {}^{3}\Delta + \sum_{l=0}^{2} {}^{4}\Delta$, where i, j, k, and l represent the number of deuterons that are bonded to the carbon ($^{1}\Delta$), or that are two ($^{2}\Delta$), three ($^{3}\Delta$), or four ($^{4}\Delta$) bonds away (these chemical shift effects would be in addition to coupling effects arising from deuterons directly bonded to ^{13}C nuclei) (Figure SI-1). For the quaternary bridgehead carbons of diol **5**-*d*, to which no deuterons may be attached, striking consequences are observed due to chemical shift effects arising from nearby ^{2}H substitution, which may be represented by the expression $\Delta\delta_{\text{bridgehead}} = \sum_{m=0}^{4} {}^{2}\Delta + \sum_{n=0}^{4} {}^{3}\Delta$, where m and n represent the possible number of deuterons that are two ($^{2}\Delta$) or three ($^{3}\Delta$) bonds away from it (Figure SI-2)

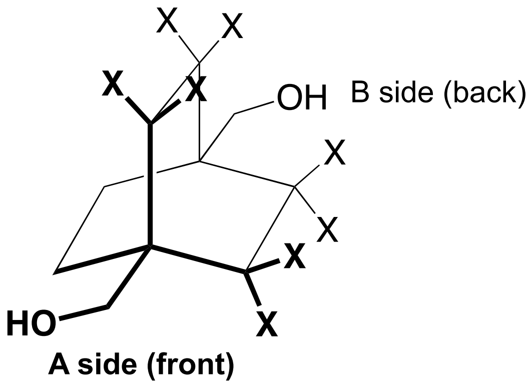

A	B
X=4 D	X=4 D
X=3 D	X=3 D
X=2 D	X=2 D
X=1 D	X=1 D
X=0 D	X=0 D

Figure SI-1. Possible statistical isotopic substitutions on in diol **5**-*d* (and similarly, for diacid **6**-*d*) . There are a number of possible interactions leading to $^{1}\Delta$, $^{2}\Delta$, $^{3}\Delta$, and $^{4}\Delta$ chemical shift deuterium isotope effects (*vide infra*). It was experimentally determined that the average total deuterium content on the ring was three.

The magnitude and origin of the ^{2}H chemical shift effects on ^{13}C nuclei have been previously characterized.[3] The smaller vibrational amplitude of a C—D bond with respect to a C—H bond results in the bonding electrons being closer, on average, to the resonating ^{13}C nucleus in the C—D bond, and hence exerts a larger shielding effect resulting in upfield shifts of $^{1}\Delta$ = 0.400 ppm and $^{2}\Delta$ = 0.100 ppm. $^{3}\Delta$ upfield chemical shifts, between 0.000 - 0.055 ppm, originate from an angular dependent, through-bond, electron-releasing effect of deuterium and a through-space interaction between the C—H(D) dipole and the γ-carbon electrons. $^{4}\Delta$ chemical shift effects of -0.014 to +0.017 ppm arise from a through space interaction of the C—H(D) dipole and the δ-carbon electrons, steric effects of deuterium, and/or a slight change in the bridge conformation resulting from ^{2}H substitution.

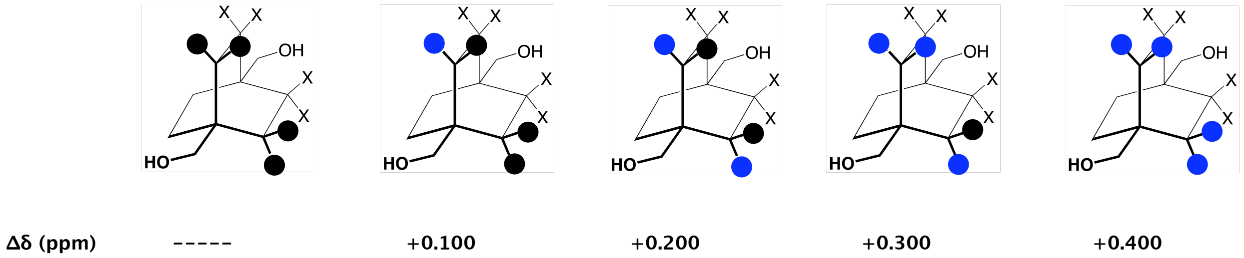

● = H (2 bonds away from bridgehead)

🔵 = D (2 bonds away from bridgehead→ ${}^2\Delta$ effects)

X = H or D (D 3 bonds away from bridgehead→ ${}^3\Delta$ effects)

Figure SI-2. For the quaternary bridgehead carbon of diol **5**-*d*, to which no deuterons may be attached, striking consequences are observed due to ^{2}H substitution arising from chemical shift effects, which may be represented by the expression $\Delta\delta_{\text{bridgehead}} = \sum_{m=0}^{4} {}^2\Delta + \sum_{n=0}^{4} {}^3\Delta$, where m and n represent the number of deuterons that are two (${}^2\Delta$) or three (${}^3\Delta$) bonds away. The magnitude of ${}^2\Delta$ = +0.100 pm is much greater than ${}^3\Delta$ = + 0.000 - 0.055 ppm, and affects less strongly the ^{13}C chemical shift (see a zoom in of this phenomenon for the bridgehead carbon of **5**-*d* in the ^{13}C NMR spectra collected at frequencies of 125 MHz and 150 MHz in Figs. A.5.7 and A.5.10, respectively). The same effects are evident in the diacid **6**-*d.*

Bicyclo[2.2.2]octane-H/D-1,4-dicarboxylic acid (BODCA) *(6-d).* **6**-*d* was prepared *via* a Jone's Oxidation of diol **5**-*d*. 141 mg (~0.81 mmol) of **5** was dissolved in 13 mL of acetone and added to a 25 mL 14/20 round bottom flask. 260 mg of CrO_3 in 0.3 mL concentrated H_2SO_4 and 2.5 mL H_2O were mixed together in a separate container, and the deep red mixture was then added to the flask drop wise while stirring. A color change from deep red to greenish blue was observed. The reaction setup was fitted with a water condenser, and the solution was refluxed for 30 min. The solution was subsequently poured into 34 mL of ice water, whereupon a white precipitate immediately formed. The precipitate was filtered and washed generously with water. The dried white powder was obtained in an isolated yield of 103 mg (~63%). ^{1}H NMR (500 MHz, CD_3OD) δ (ppm): 1.81 (s), 1.80 (s), 1.79 (s). ^{13}C NMR (125MHZ, CD_3OD) δ (ppm):

181.51, 39.56, 39.48, 39.40, 39.31, 28.96, 28.94, 28.91, 28.85, 28.80, 28.43 (p, 19.8 Hz, split due to $^1\Delta$, $^2\Delta$, $^3\Delta$, and $^4\Delta$ ^{2}H chemical shift isotope effects of *ca*. 6.5 Hz. ATR FT-IR (cm^{-1}): 2956.34, 2880.95, 2813.49, 2638.88, 2527.77, 1682.44, 1411.23, 1298.23, 1274.44, 1088.10, 955.28. Liquid Introduction Field Desorption Ionization Mass Spectrometry (*m*/*z*): M$^+$ 198 (D_0), 199 (D_1), 200 (D_2), 201 (D_3), 202 (D_4), 203 (D_5), 204 (D_6). The natural abundance **6** was prepared in an analogous fashion to **6**-*d* *via* the Jones Oxidation, starting from natural abundance diol **5**. ^{1}H NMR (300 MHz, $SO(CD_3)_2$ δ (ppm): 1.67. ^{13}C NMR (500 MHZ, CD_3OD) δ (ppm): 178.91, 38.08, 27.90. ATR FT-IR (cm^{-1}): 2960.31, 2876.98, 2619.04, 2531.74, 1684.80, 1458.81, 1411.23, 1302.30, 1274.44, 1092.07, 953.30, 751.10.

Scheme SI-2. One-pot synthesis of BODCA MOF, where red represents the dynamic rotator moieties and blue represents the static carboxylate and ligand clusters relative to the rotator.

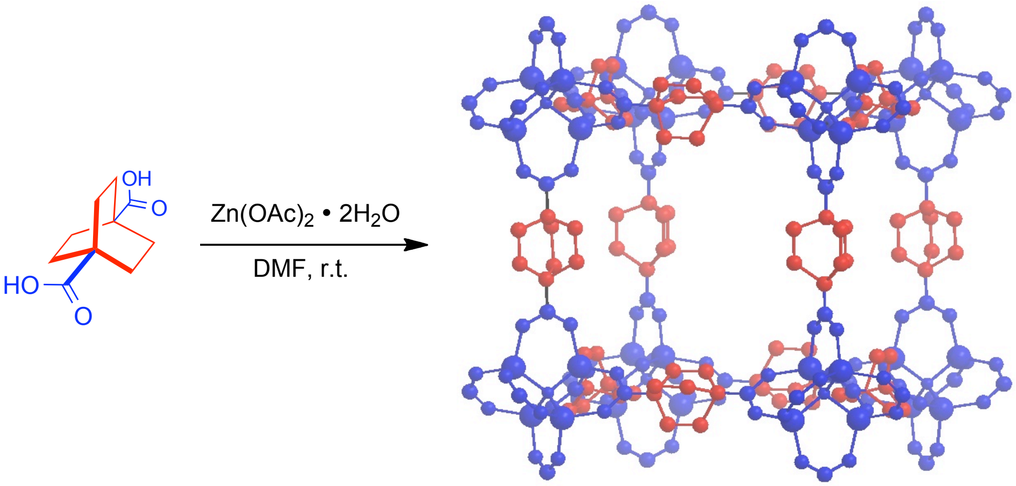

Bicyclo[2.2.2]octane-H/D-1,4-dicarboxlate metal-organic framework (BODCA MOF).

In an oven-dried glass vial fitted with a Teflon-lined plastic cap, 100 mg (0.5 mmol) of BODCA ligand **6** was dissolved in 4 mL DMF and the cap was quickly replaced. To a separate oven-dried glass vial fitted with a Teflon-lined plastic cap and a stir bar was added 320 mg (1.5 mmol) of zinc acetate dihydrate and 4 mL of dry DMF and the cap was quickly replaced. After complete dissolution of the solids in the two separate vials, solution **6** was added dropwise to the zinc acetate solution while stirring, resulting in the formation of a white precipitate. After addition, the cap was quickly replaced and the milky white solution was stirred for an additional 15 min. The solution was then left to stand, unagitated. After 15 h, the mixture was separated by centrifugation and the mother liqueur was decanted and replaced with 5 mL DMF, taking care to quickly recap after the addition. The mixture was agitated to re-disperse the white solid, and then it was separated by centrifugation. This washing process was immediately repeated two more times. Following the DMF washing, the white solid was then dispersed in dichloromethane, agitated, and then left to sit for 48 h. After 48 h, the mixture was separated by centrifugation and the dichloromethane was decanted and replaced with 5 mL fresh dichloromethane, taking care to quickly recap after the addition. The mixture was agitated to re-disperse the white solid, and then it was separated by centrifugation. This washing process was immediately repeated one more time. Finally, most of the dichloromethane was decanted to obtain a pasty white solid. The remaining dichloromethane was removed *via* reduced pressure at room temperature. The sample was allowed to sit under reduced pressure over night at room temperature, followed by heating at 40 ºC for two hours. Finally, the sample was back filled with He(*g*) to obtain the BODCA MOF as a white polycrystalline powder before sealing in a capillary for ^{1}H T_1 and ^{2}H spin-echo wide-line solid-state NMR experiments. In order to obtain the ^{13}C CP/MAS SSNMR spectrum, the sample was sandwiched between layers of anhydrous $MgSO_4$ in a 4 mm (outside) zirconia rotor in order to prevent decomposition due to ambient moisture. (75 MHz, MAS= 10 kHz, contact time = 5.0 ms, recycle delay = 40 s) δ (ppm): 188.37, 40.43, 28.23. ATR FT-IR (cm^{-1}): 2944.24, 2873.01, 1595.64, 1425.41, 111.89, 828.41, 751.10. The dinitrogen adsorption isotherm revealed uptake behavior characteristic of a Type II isotherm, with a BET surface area of S_{BET} = 2150 m^2 g^{-1} and a total pore volume of $V_{p,\mathrm{DR}}$ = 0.8630 cm^3 g^{-1}. Thermal gravimetric analysis showed mass loss/decomposition beginning at T > 450 ºC, suggesting that total activation of the MOF, *i.e.* the complete absence of solvent guest molecules.

SPECTRAL DATA

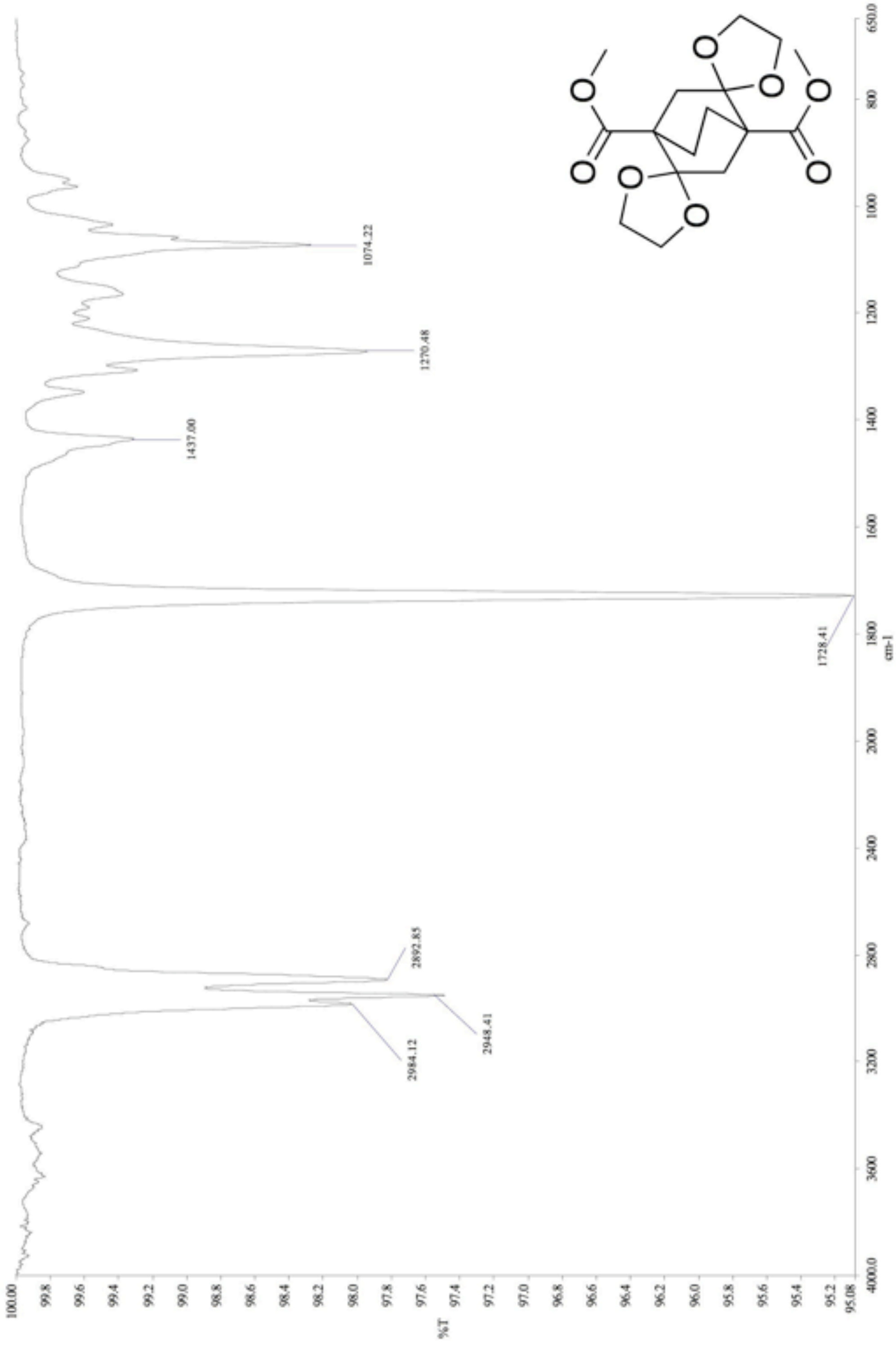

Figure SI-3. ATR FT-IR spectrum of **2**

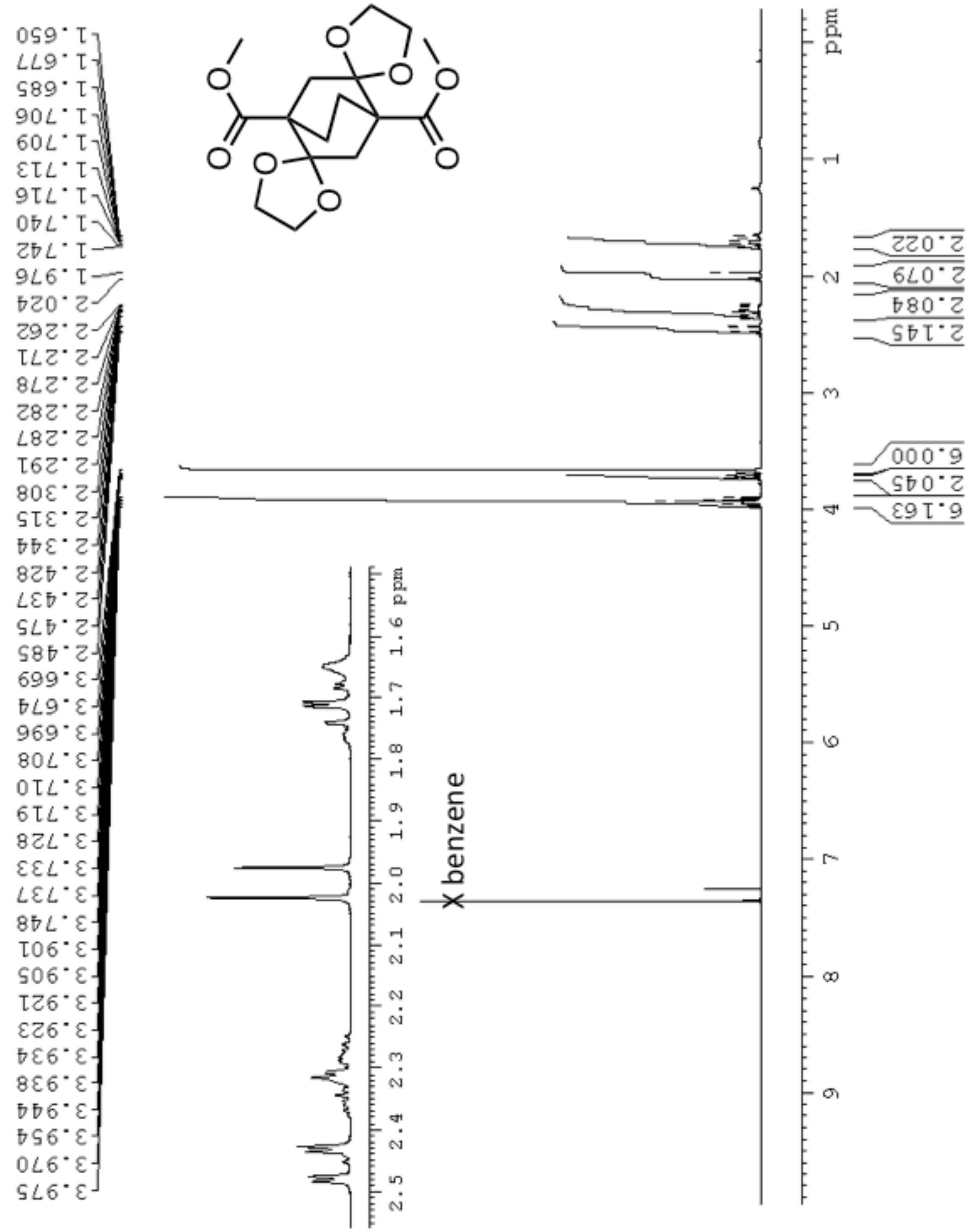

Figure SI-4. ^{1}H NMR ($CDCl_3$, 300 MHz) spectrum of **2**.

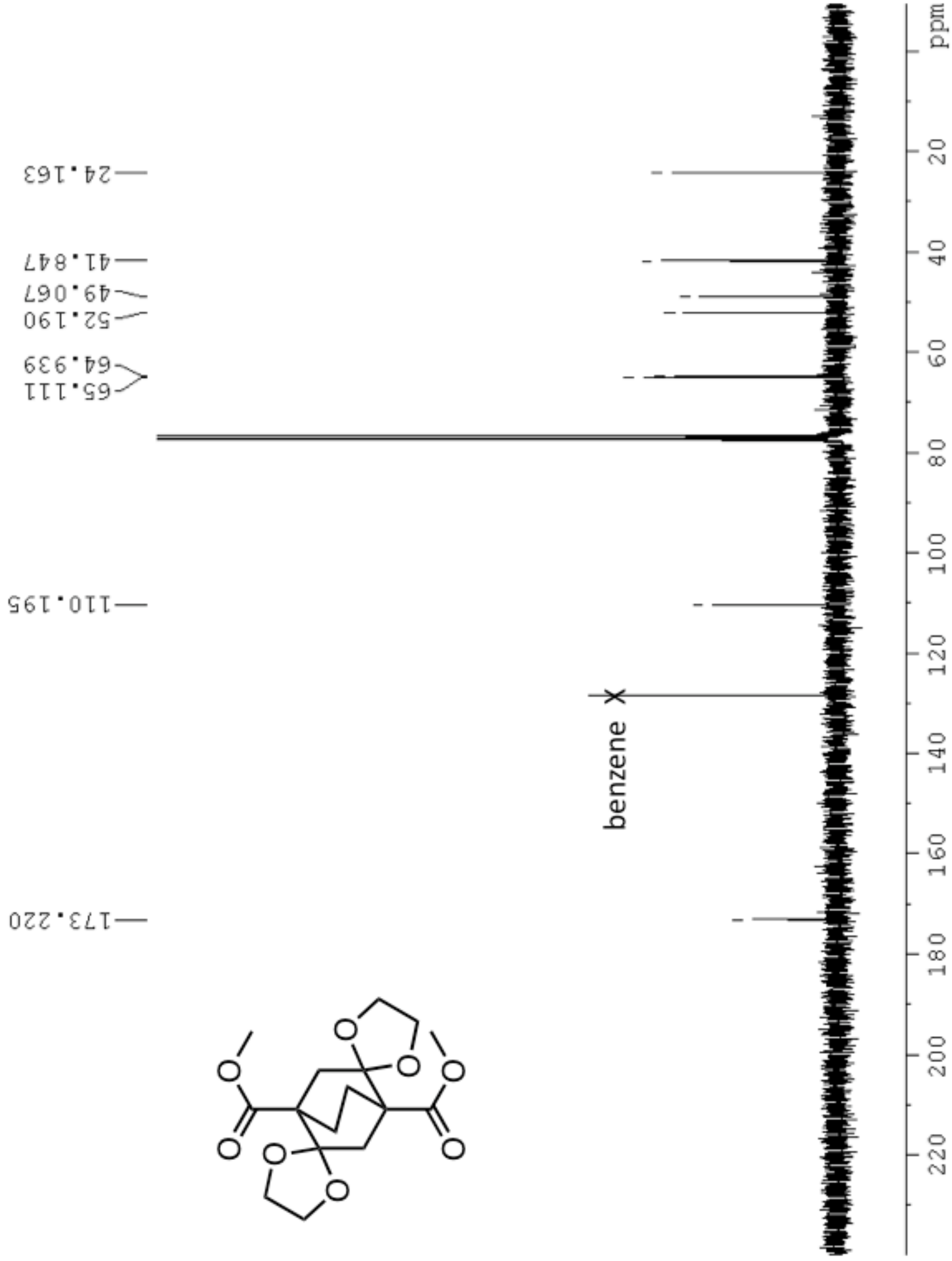

Figure SI-5. ^{13}C NMR (CDCl$_3$, 75 MHz) spectrum of **2**.

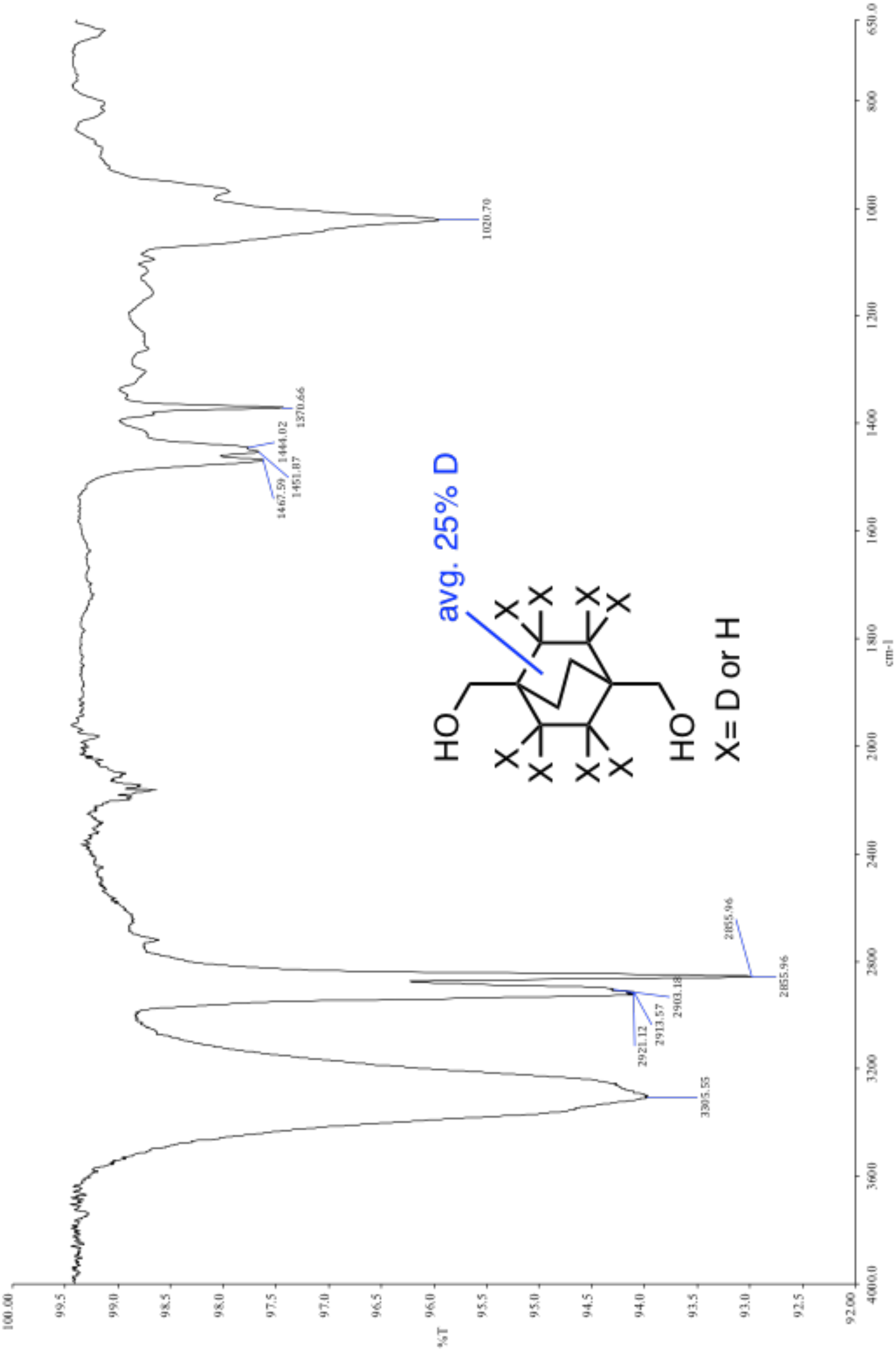

Figure SI-6. ATR FT-IR spectrum of **5**-*d*.

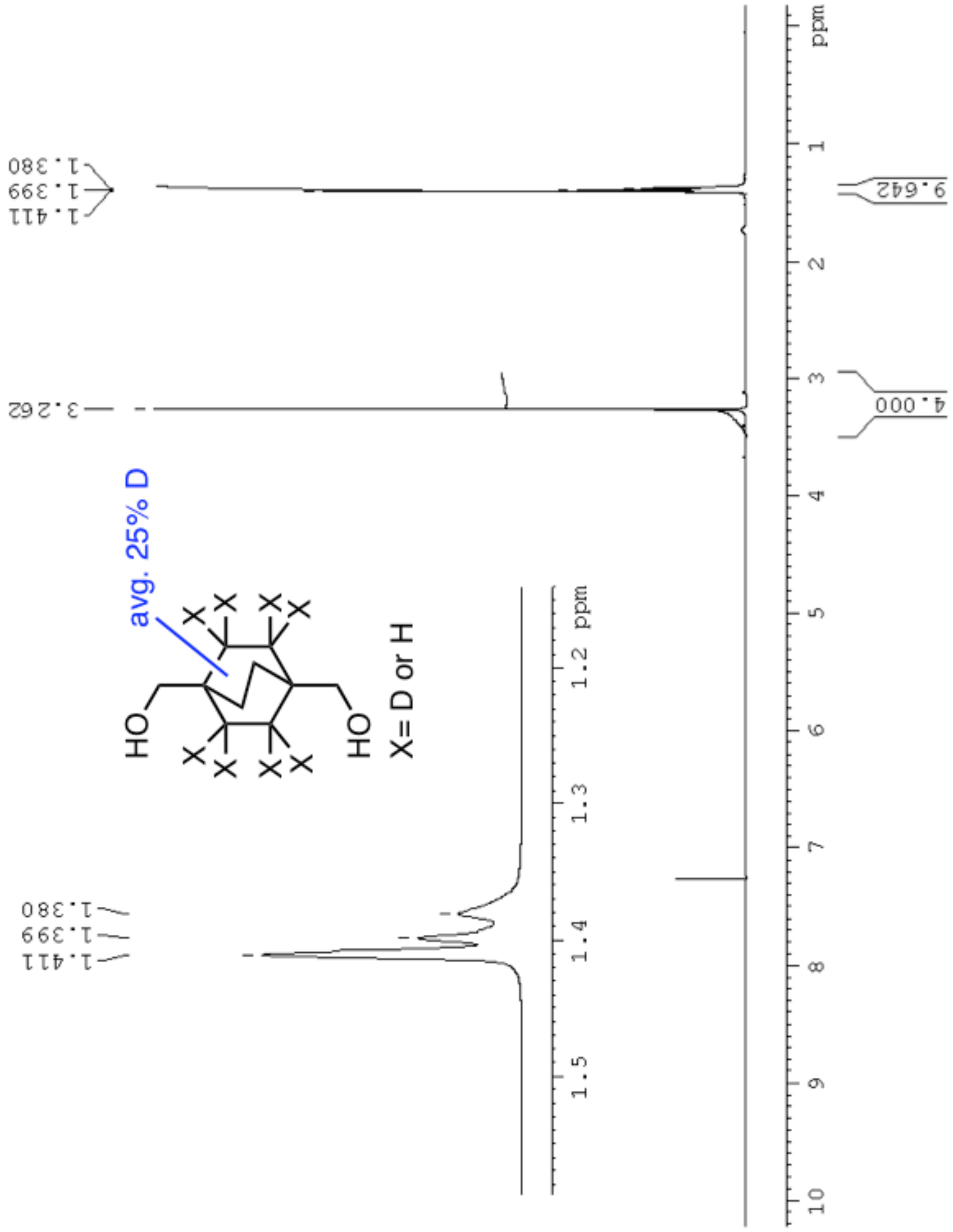

Figure SI-7 ^{1}H NMR (CDCl$_3$, 500 MHz) spectrum of **5**-*d*.

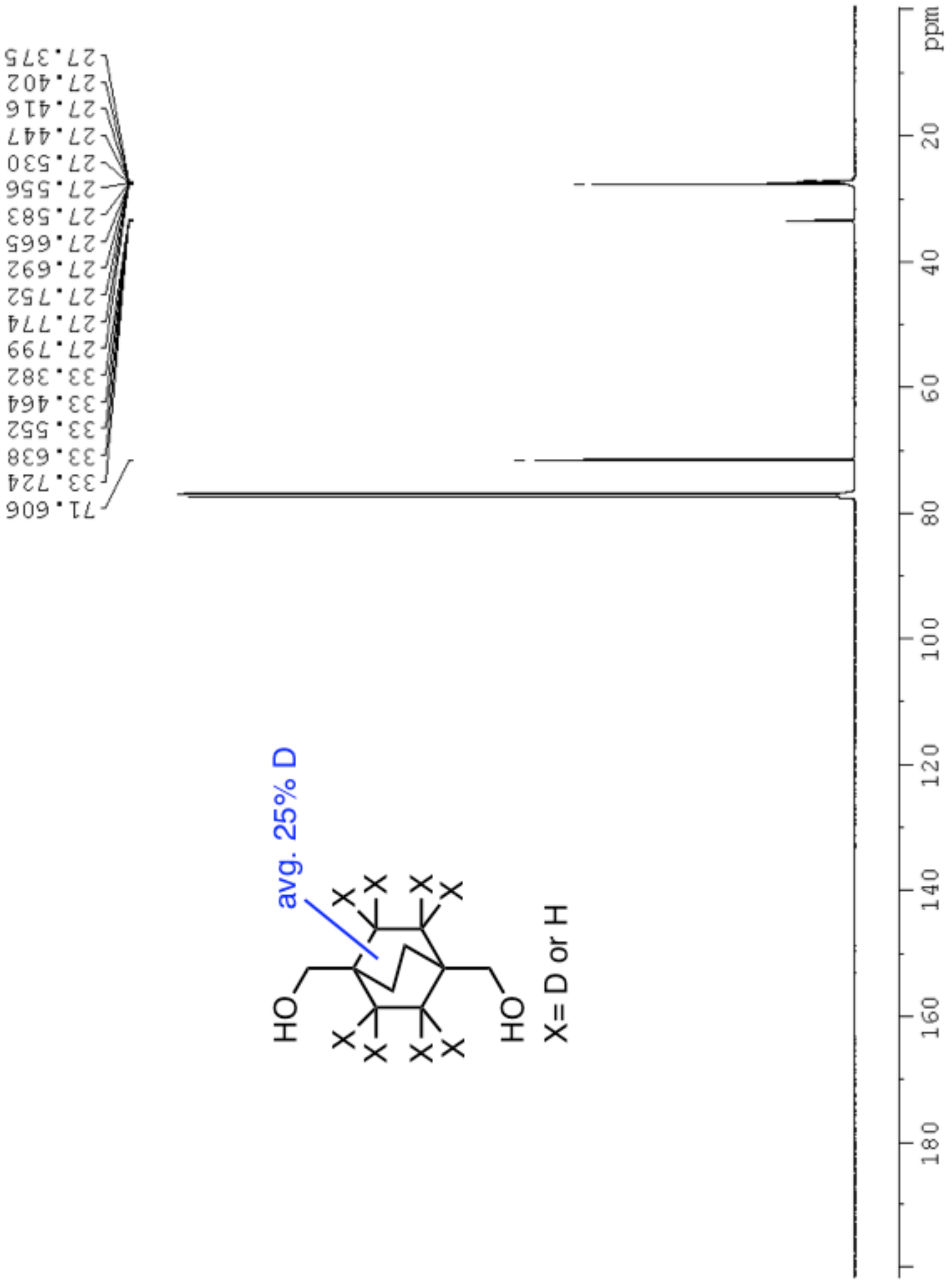

Figure SI-8. ^{13}C NMR (CDCl$_3$, 125 MHz) spectrum of **5**-*d* (full spectrum, see next figure for zoom in).

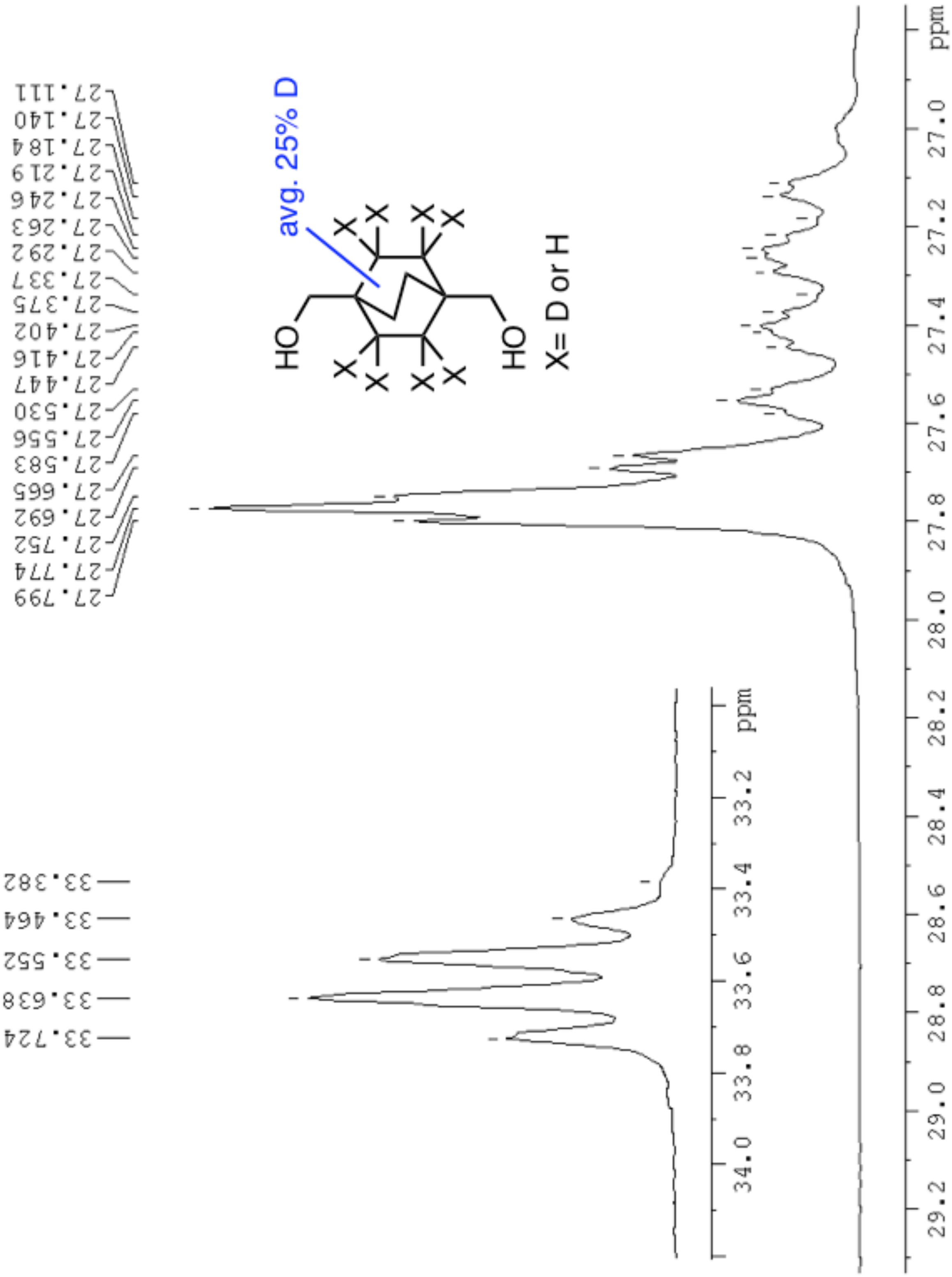

Figure SI-9. ^{13}C NMR ($CDCl_3$, 125 MHz) spectrum of **5**-*d* (zoom in of C—^{2}H coupling and ^{2}H isotope effects on the ^{13}C chemical shift).

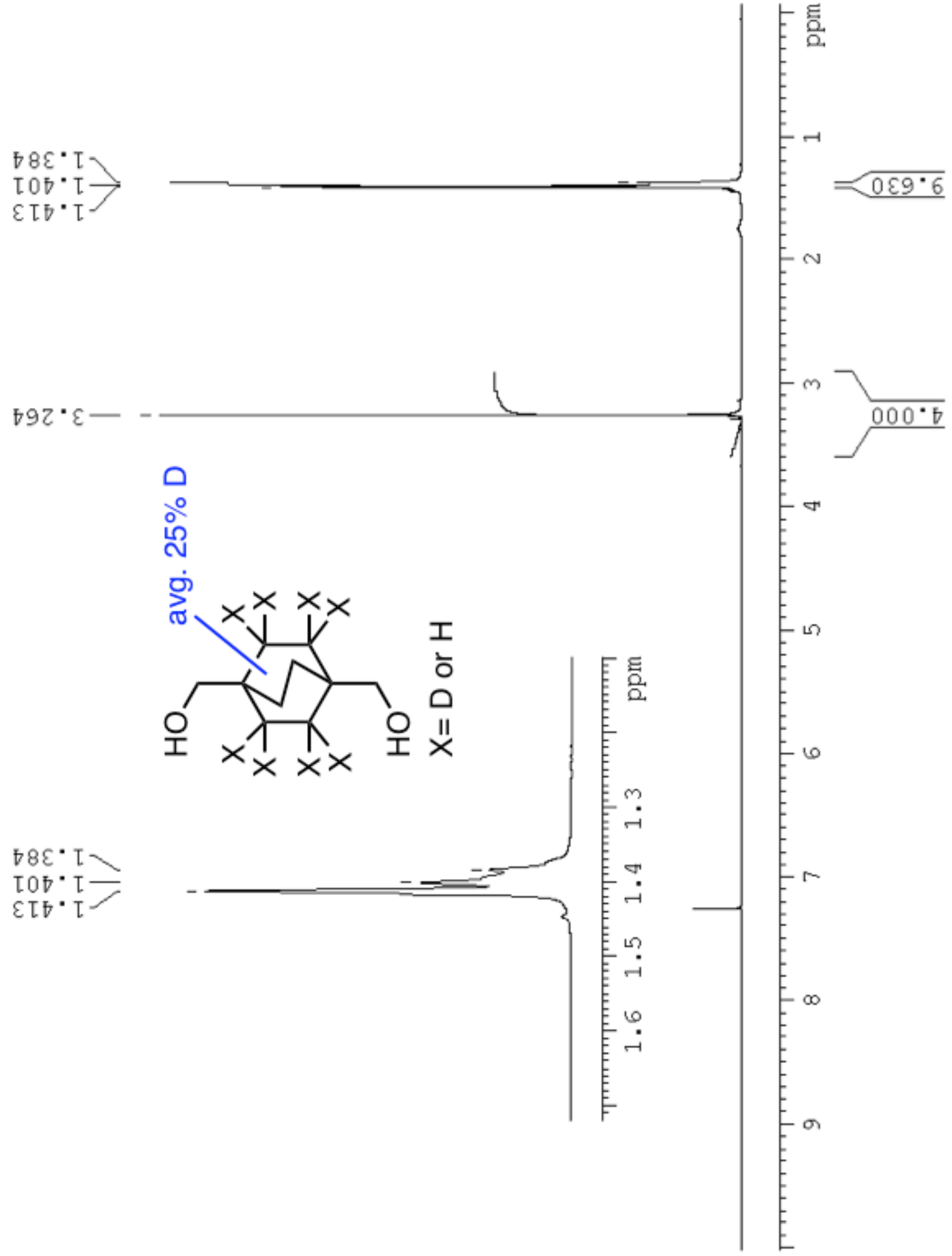

Figure SI-10. ^{1}H NMR (CDCl$_3$, 600 MHz) spectrum of **5**-*d*.

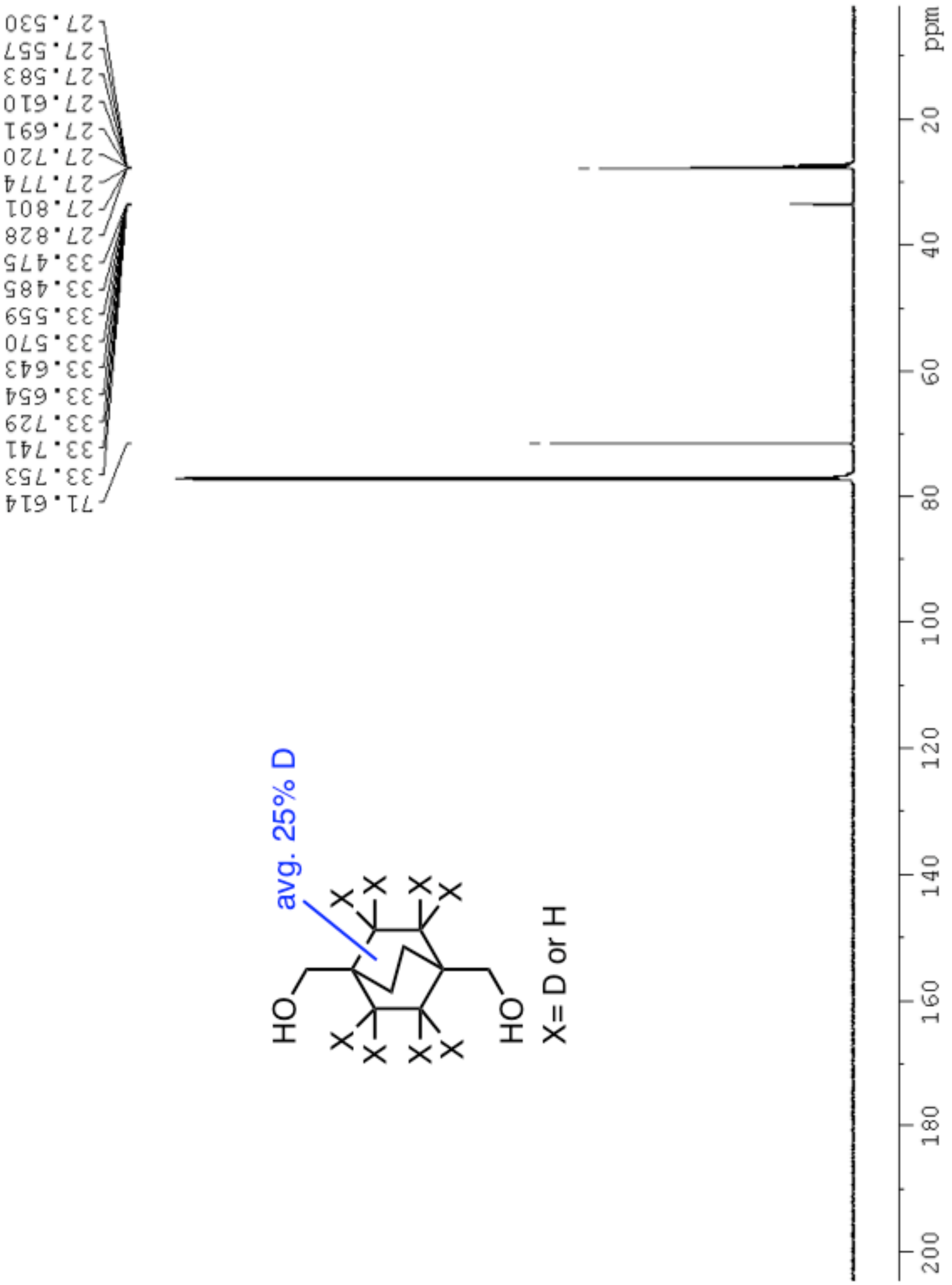

Figure SI-11. ^{13}C NMR (CDCl$_3$, 125 MHz) spectrum of **5**-*d* (full spectrum, see below for zoom in).

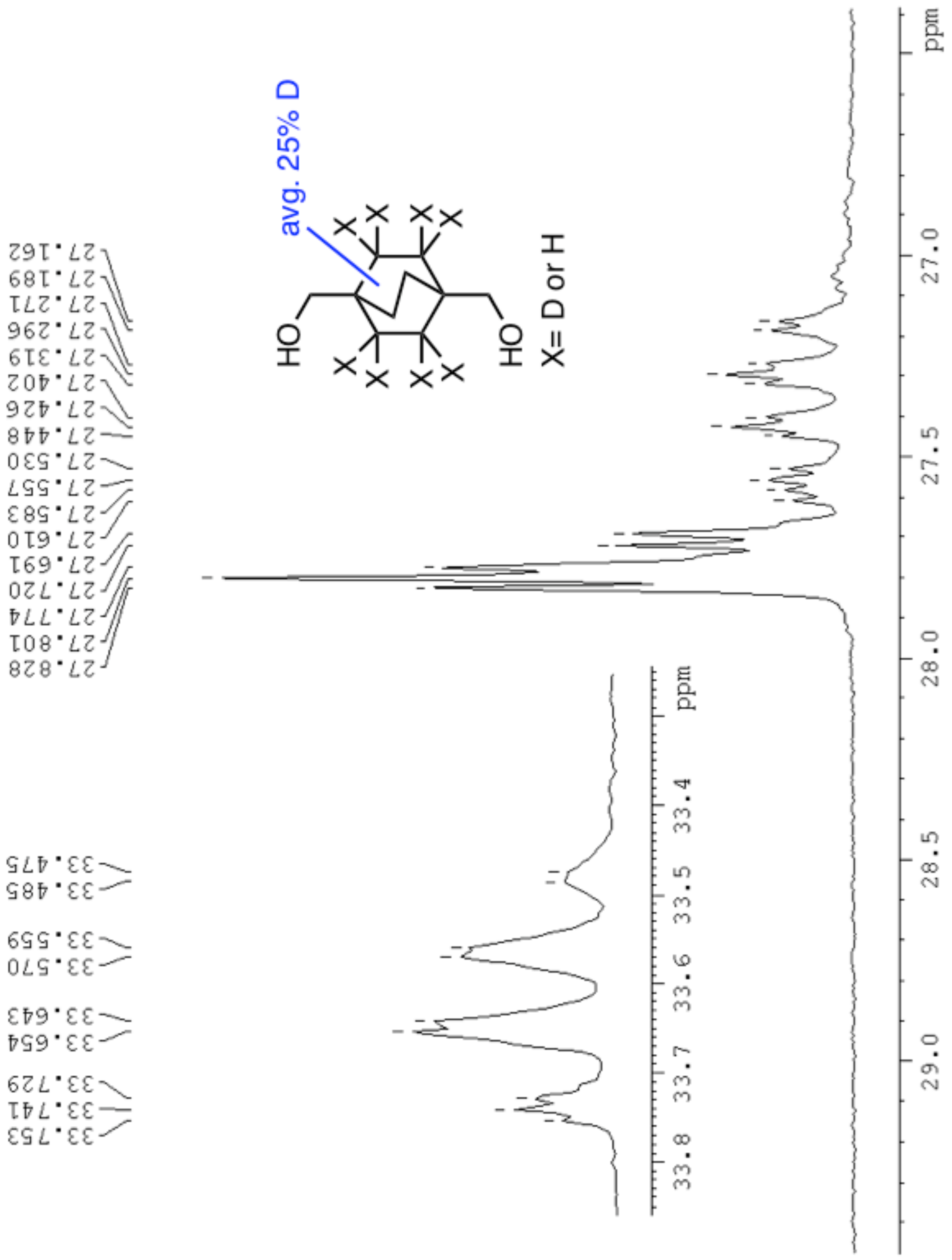

Figure SI-12. ^{13}C NMR (CDCl$_3$, 150 MHz) spectrum of **5**-*d* (zoom in of C—^{2}H coupling and ^{2}H isotope effects on the ^{13}C chemical shift).

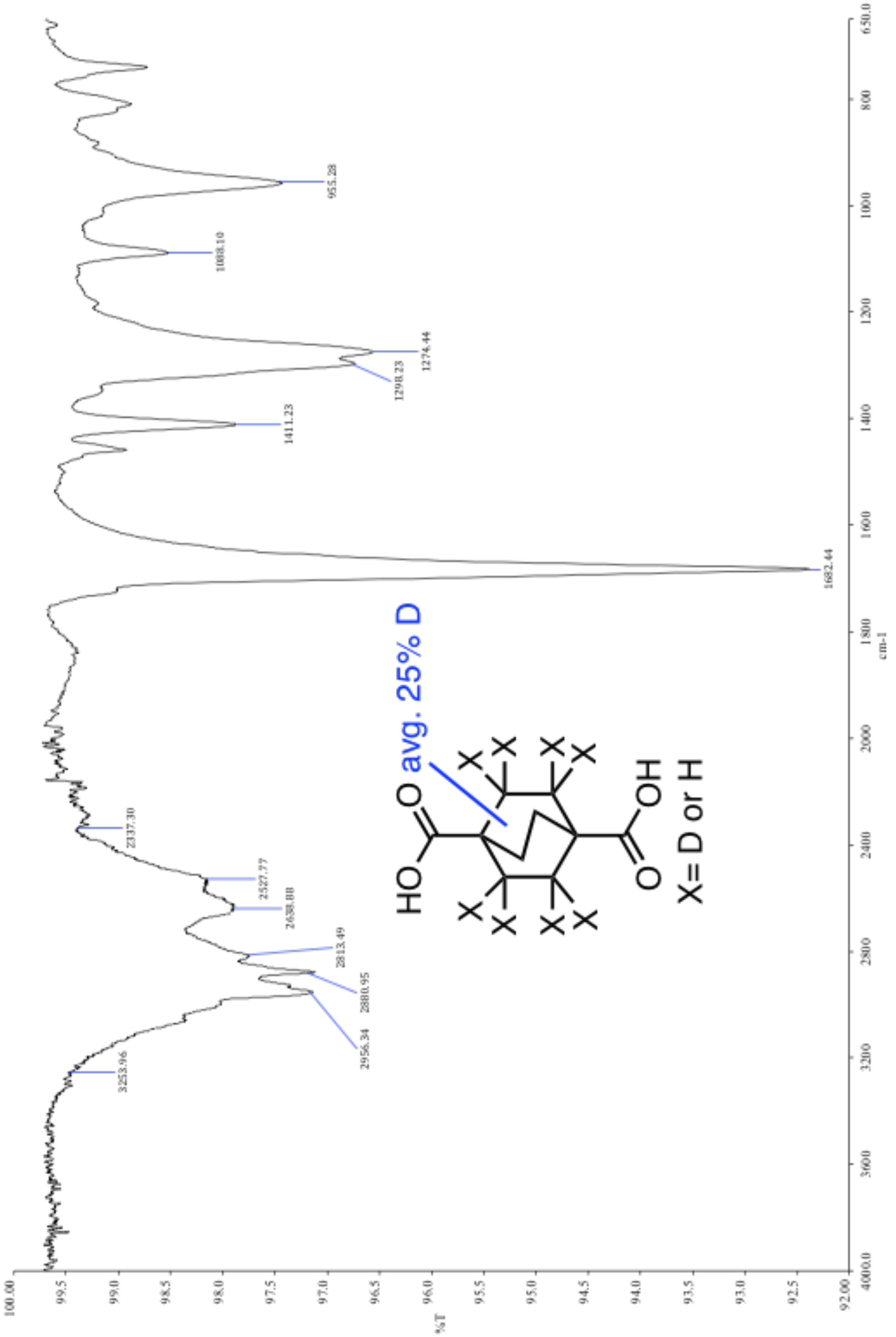

Figure SI-13. ATR FT-IR spectrum of **6**-*d*.

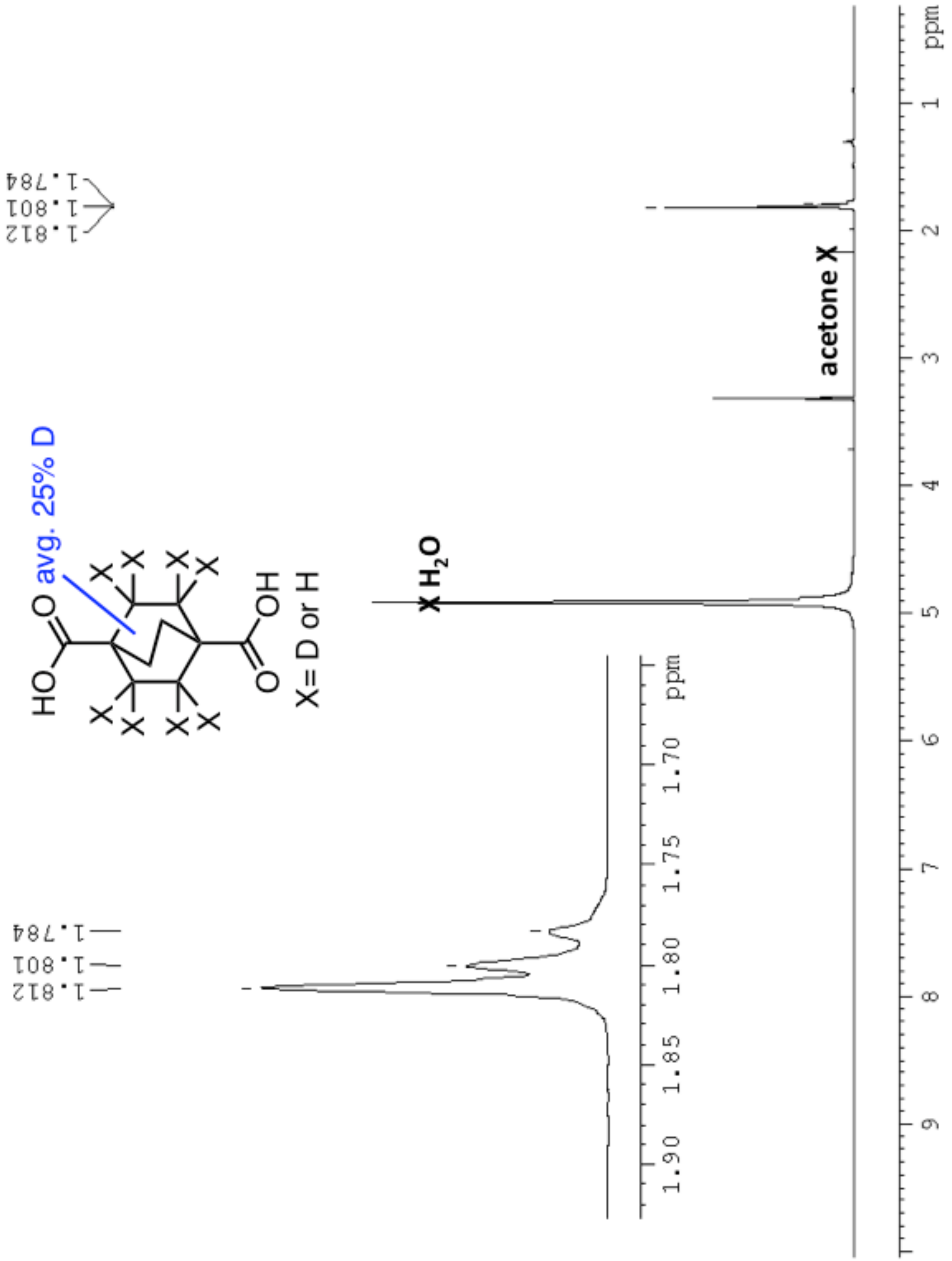

Figure SI-14. ^{1}H NMR (CD_3OD, 500 MHz) spectrum of **6**-*d*

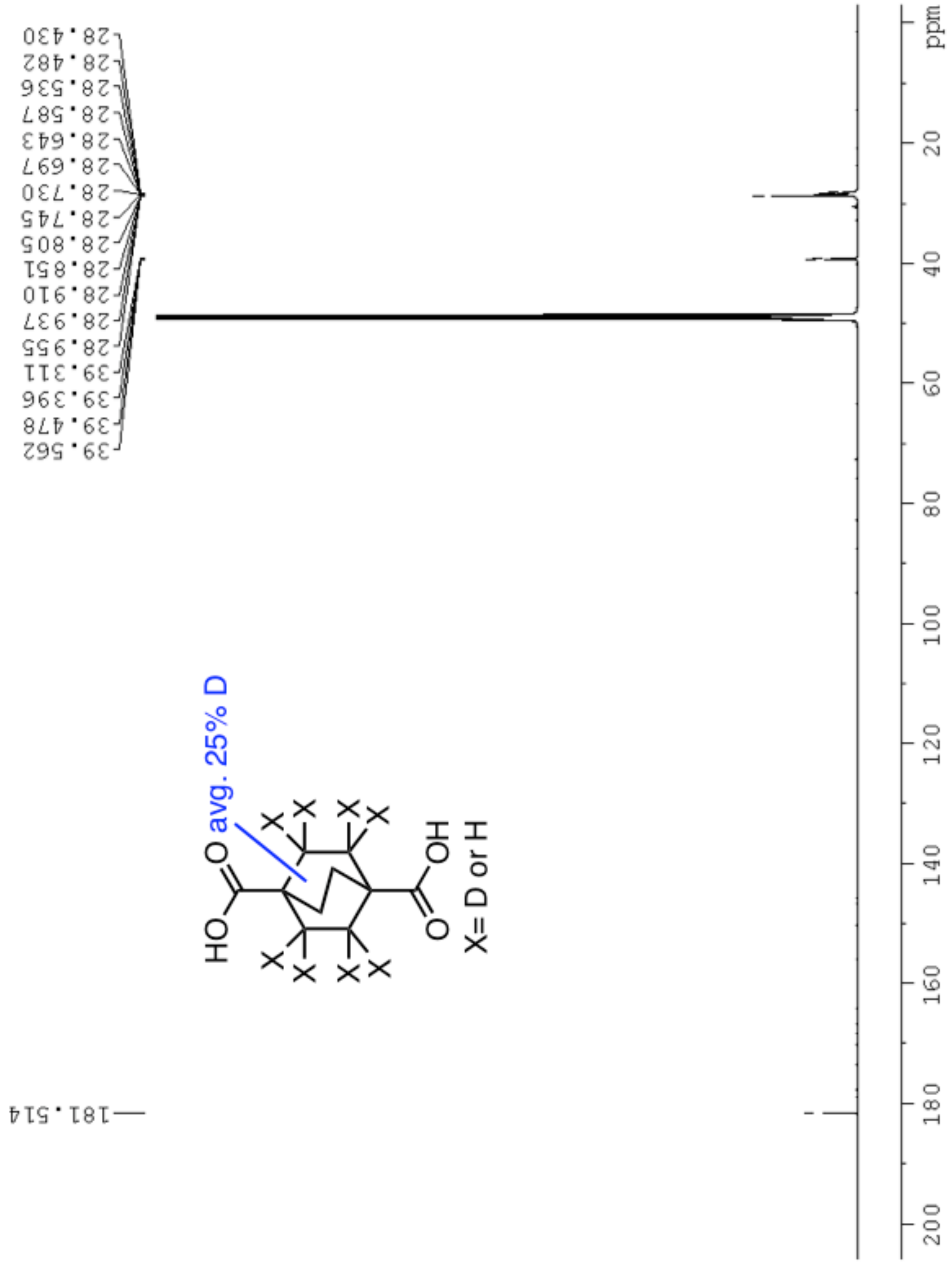

Figure SI-15. ^{13}C NMR (CD_3OD, 125 MHz) spectrum of **6**-*d*

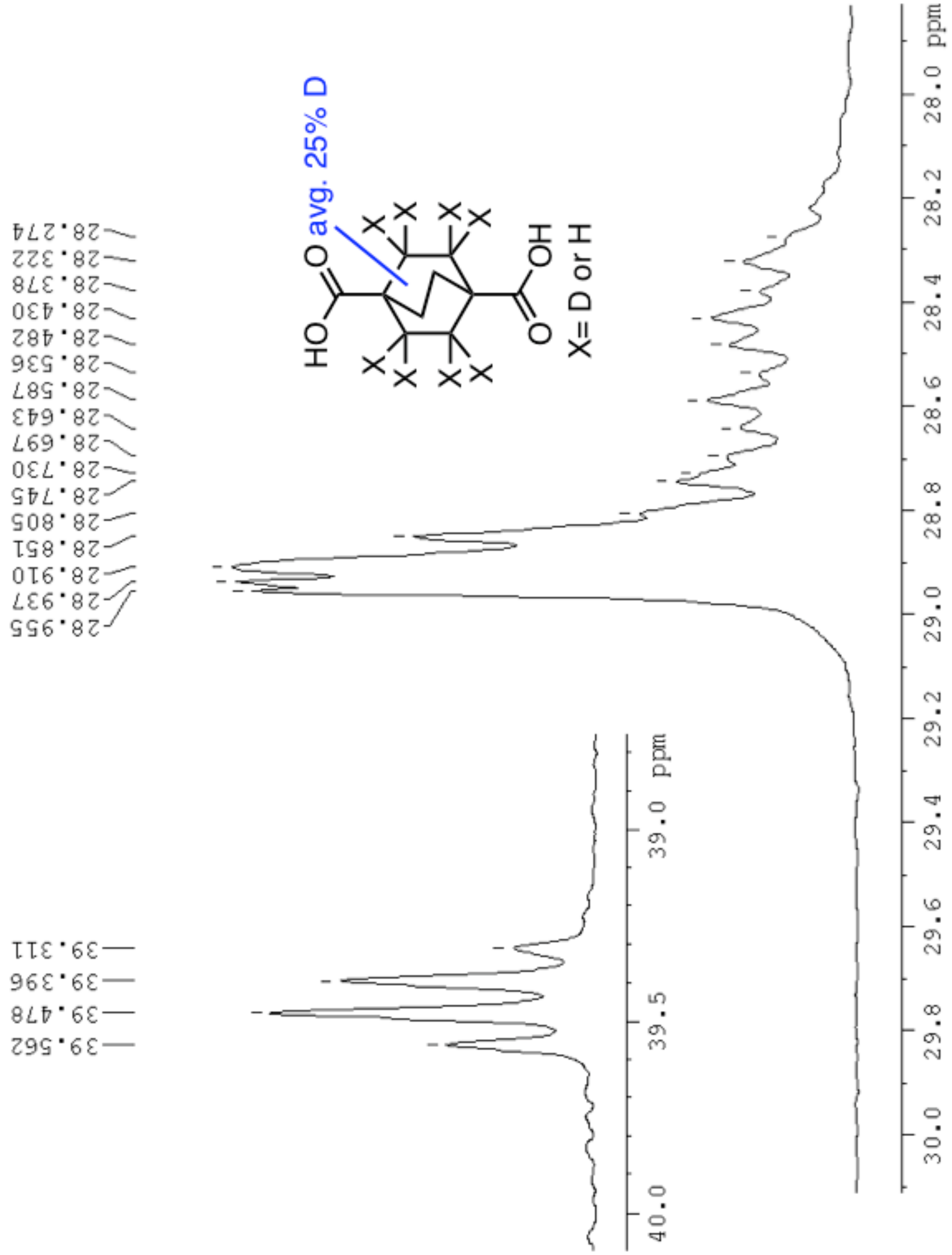

Figure SI-16 ^{13}C NMR (CD_3OD, 125 MHz) spectrum of **6**-*d*.

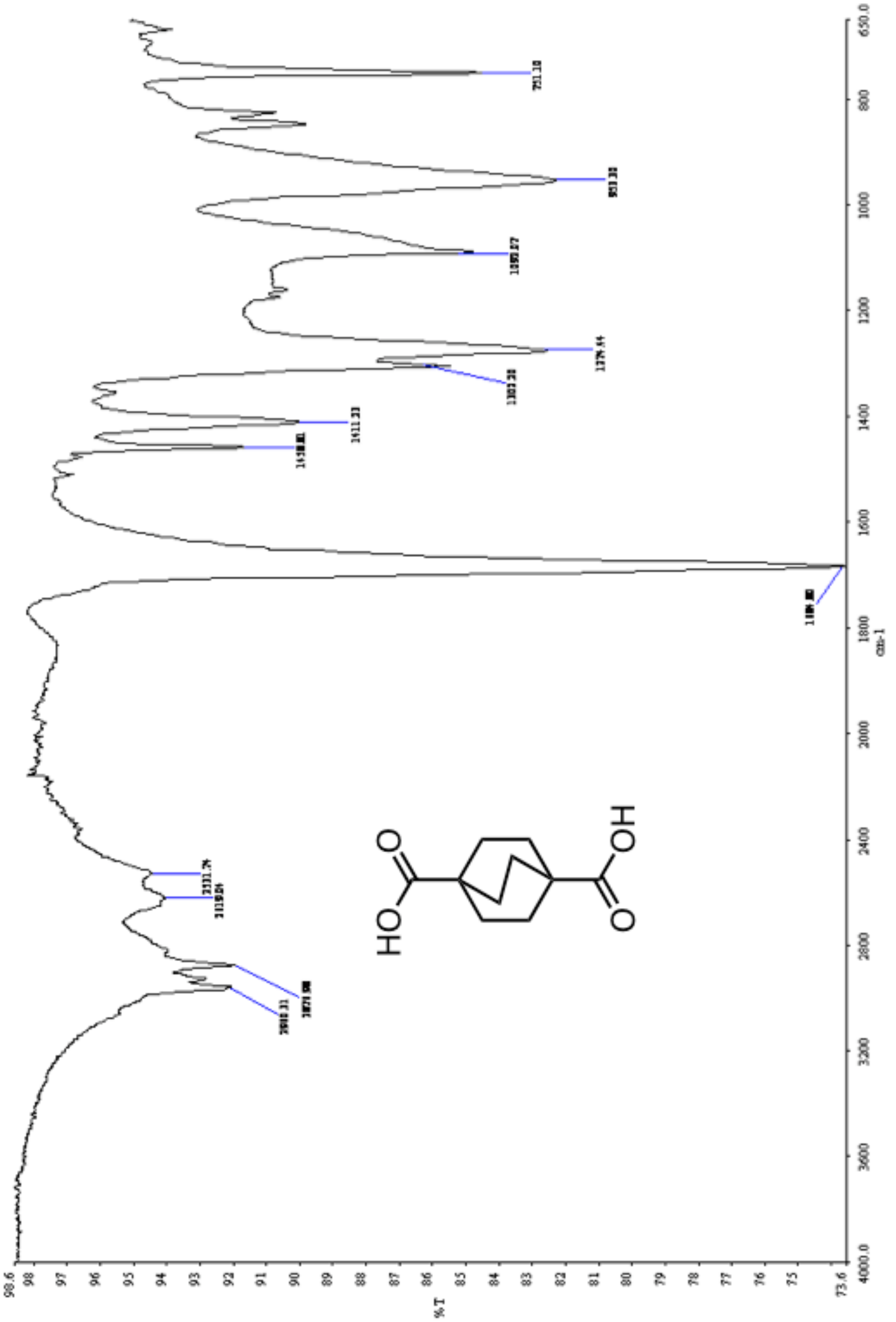

Figure SI-17. ATR FT-IR spectrum of **6**.

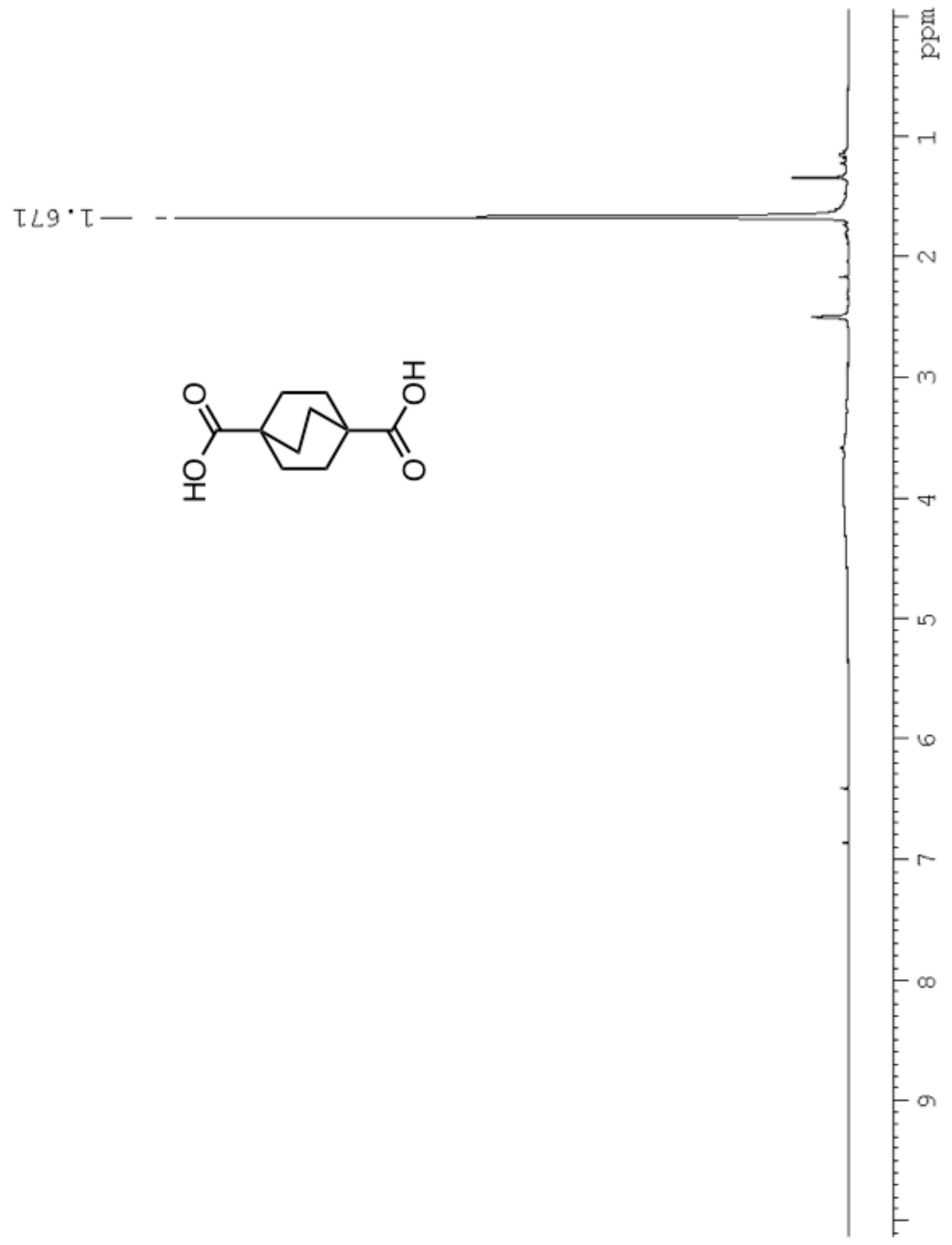

Figure SI-18. ^{1}H NMR ($SO(CD_3)_2$, 300 MHz) spectrum of **6**.

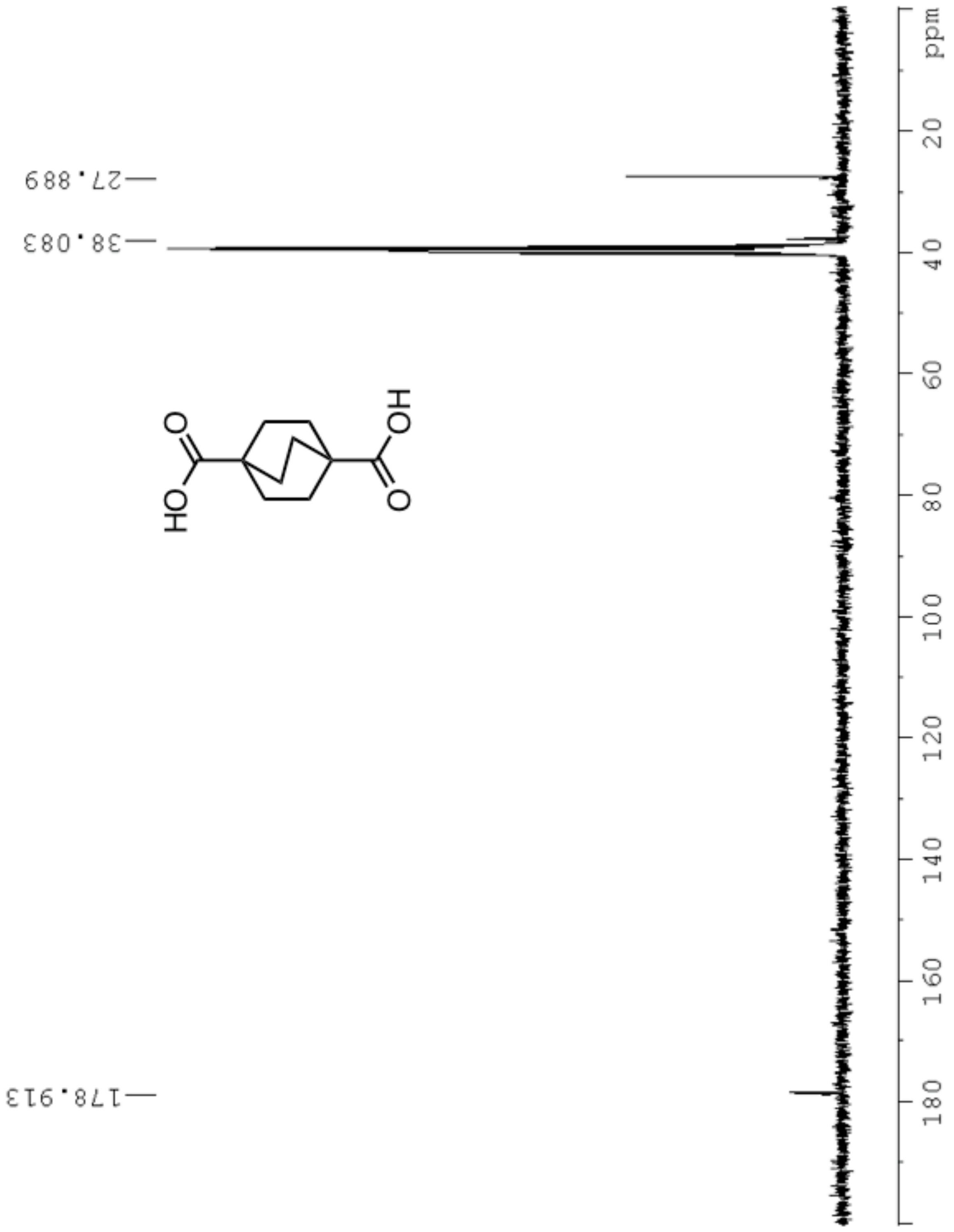

Figure SI-19. ^{13}C NMR ($SO(CD_3)_2$, 75 MHz) spectrum of **6**.

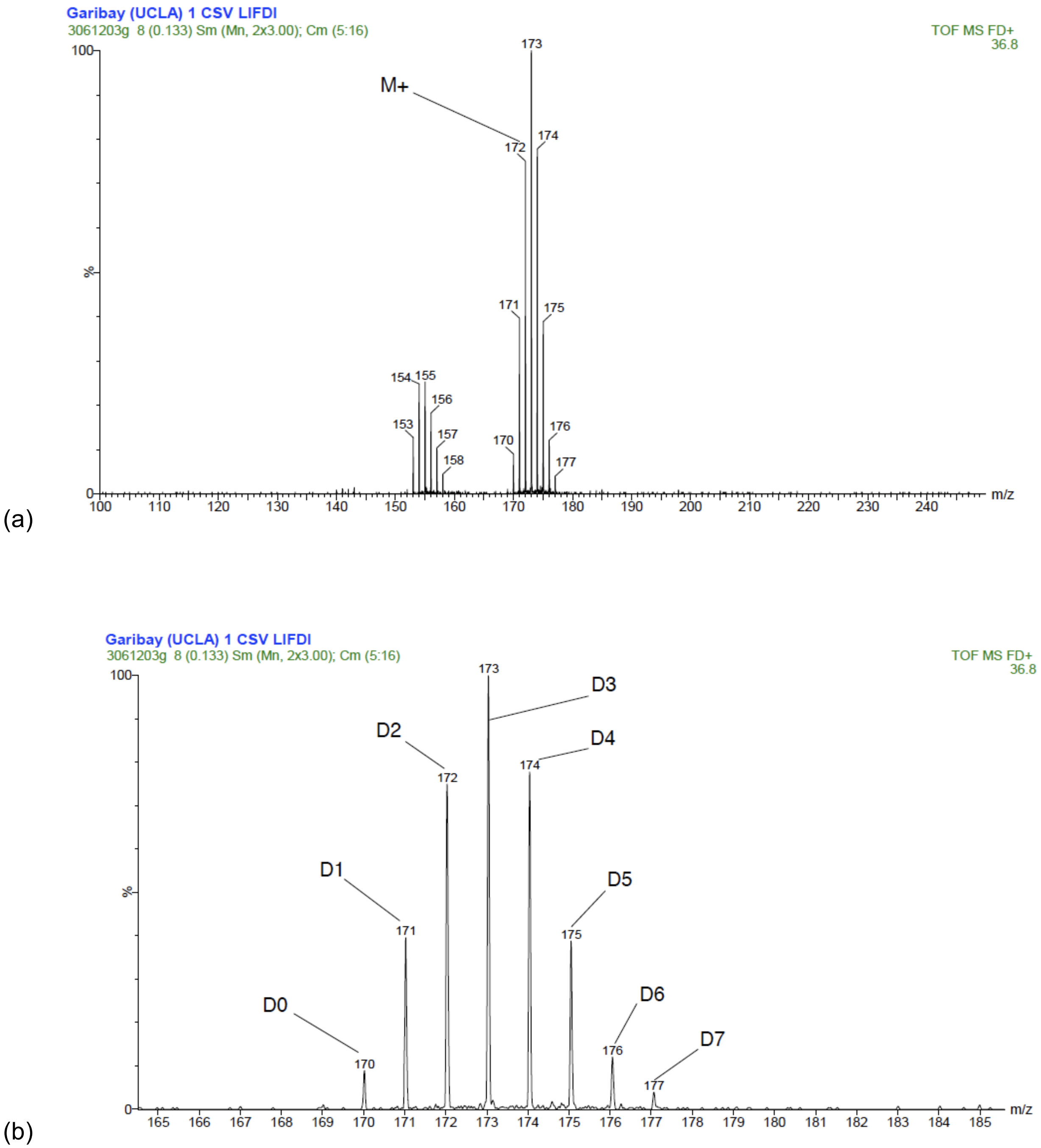

Figure SI-20. Liquid introduction field desorption ionization (LIFDI) mass spectrum of **5**-*d*. (a) Zoom out. (b) Zoom in to molecular ion, with peaks corresponsing to varying degrees of deuteron substitution.

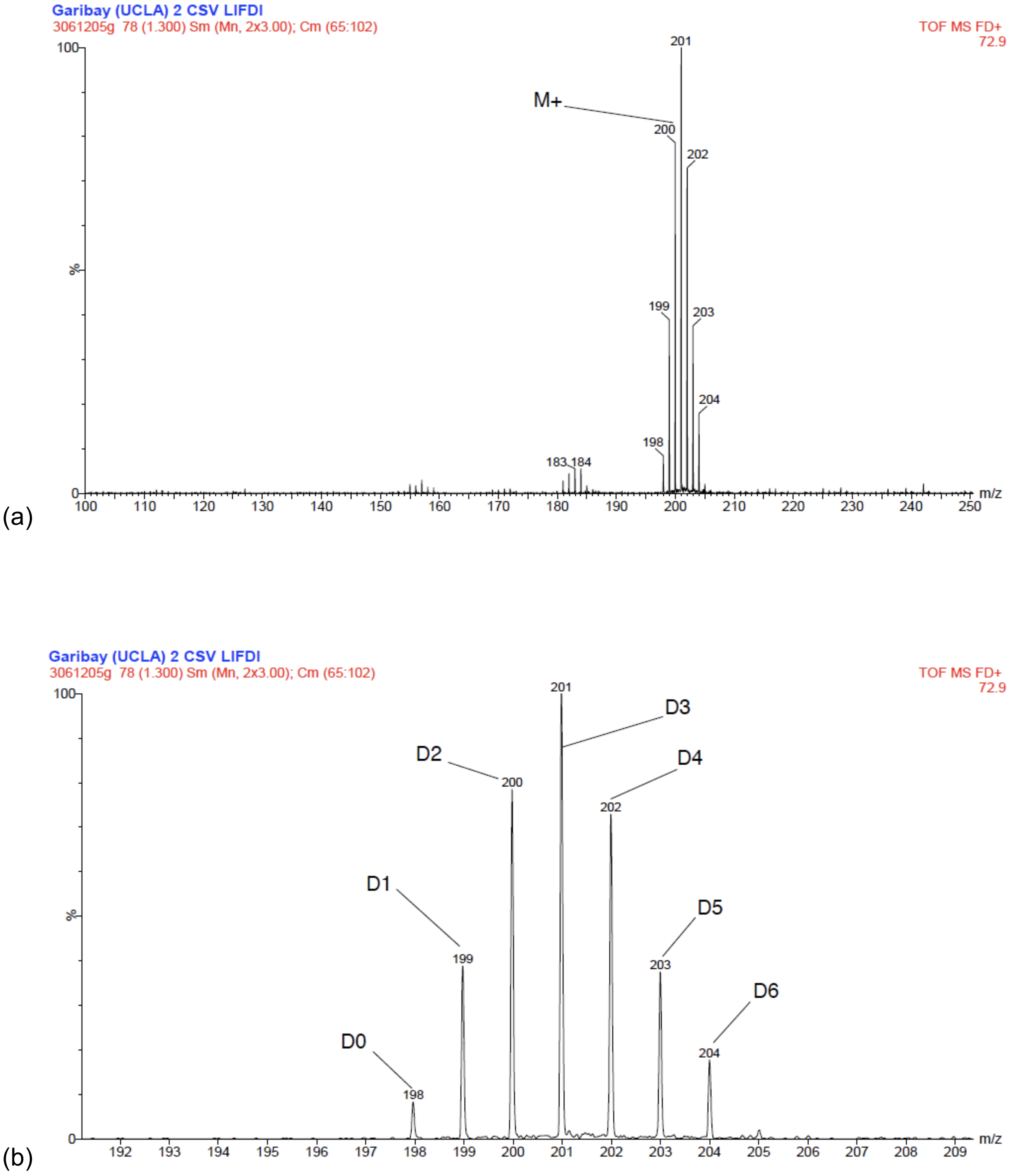

Figure SI-21. Liquid introduction field desorption ionization (LIFDI) mass spectrum of **6**-*d*. (a) Zoom out. (b) Zoom in to molecular ion, with peaks corresponsing to varying degrees of deuteron substitution.

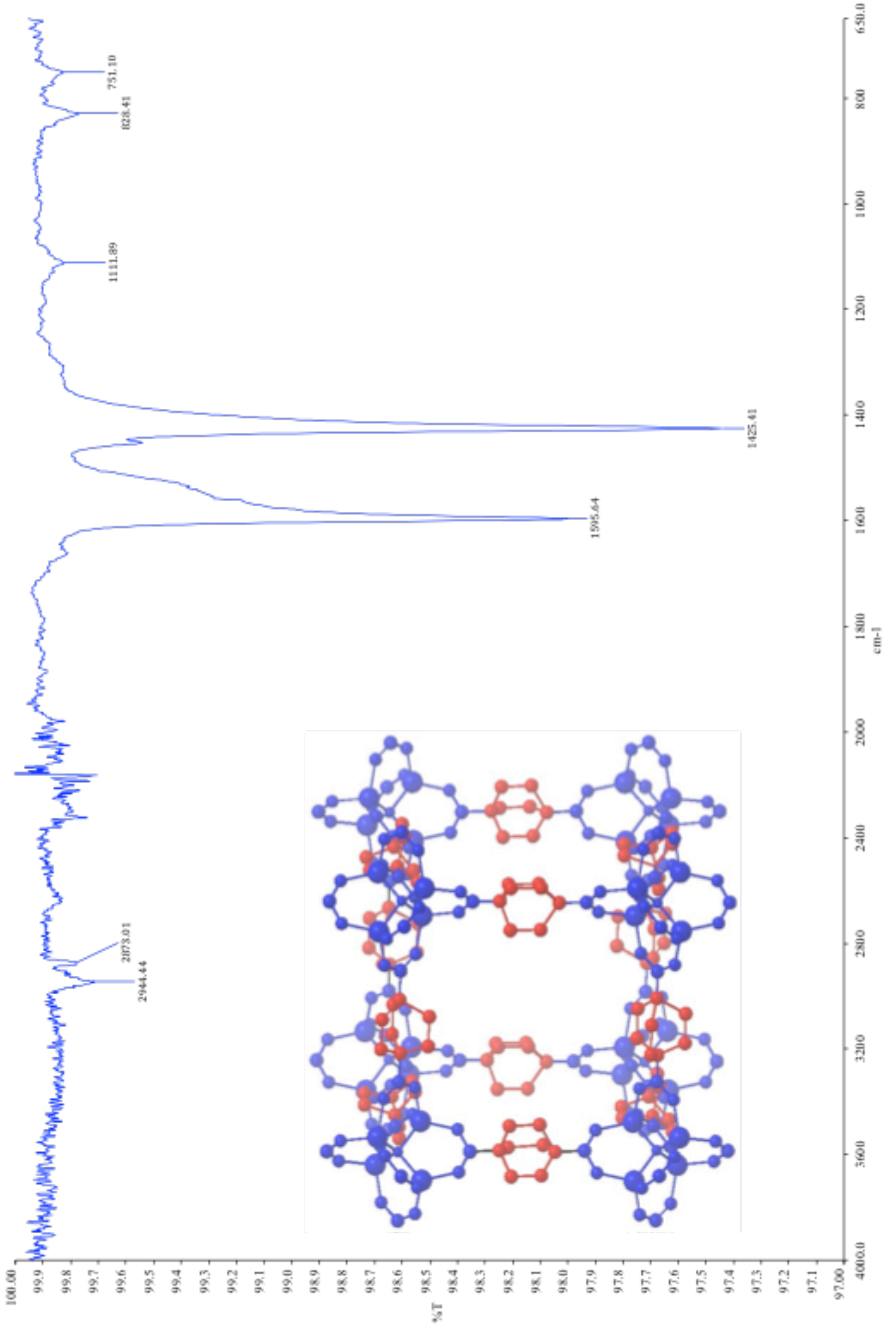

Figure SI-22. Activated BODCA MOF ATR FT-IR spectrum.

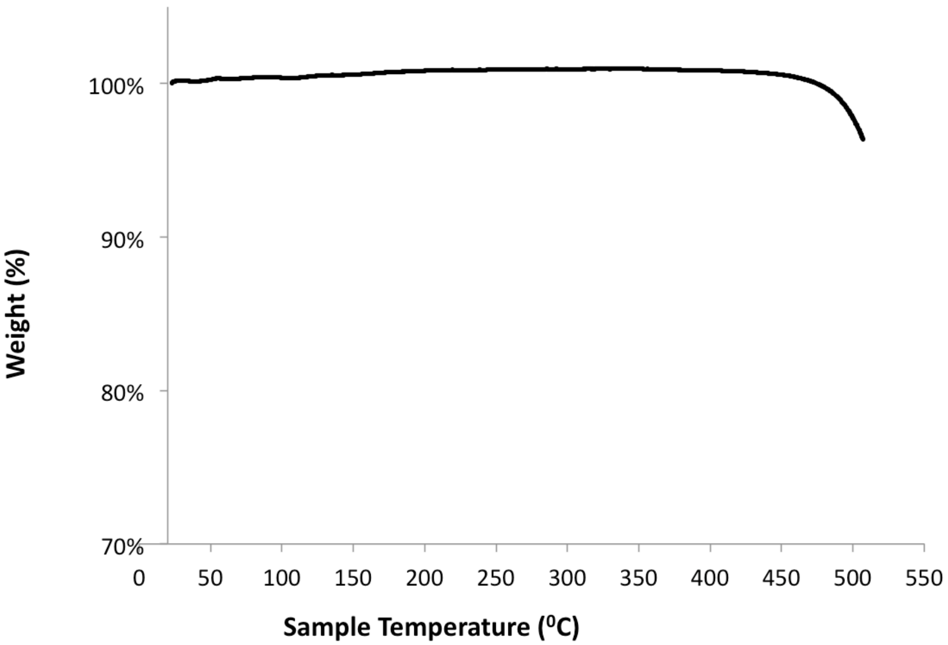

Figure SI-23 Freshly activated BODCA MOF thermogravimertic analysis. (2.955 mg of sample, ramp rate = 25.00°C to 505.00°C at 5.00°C/min).

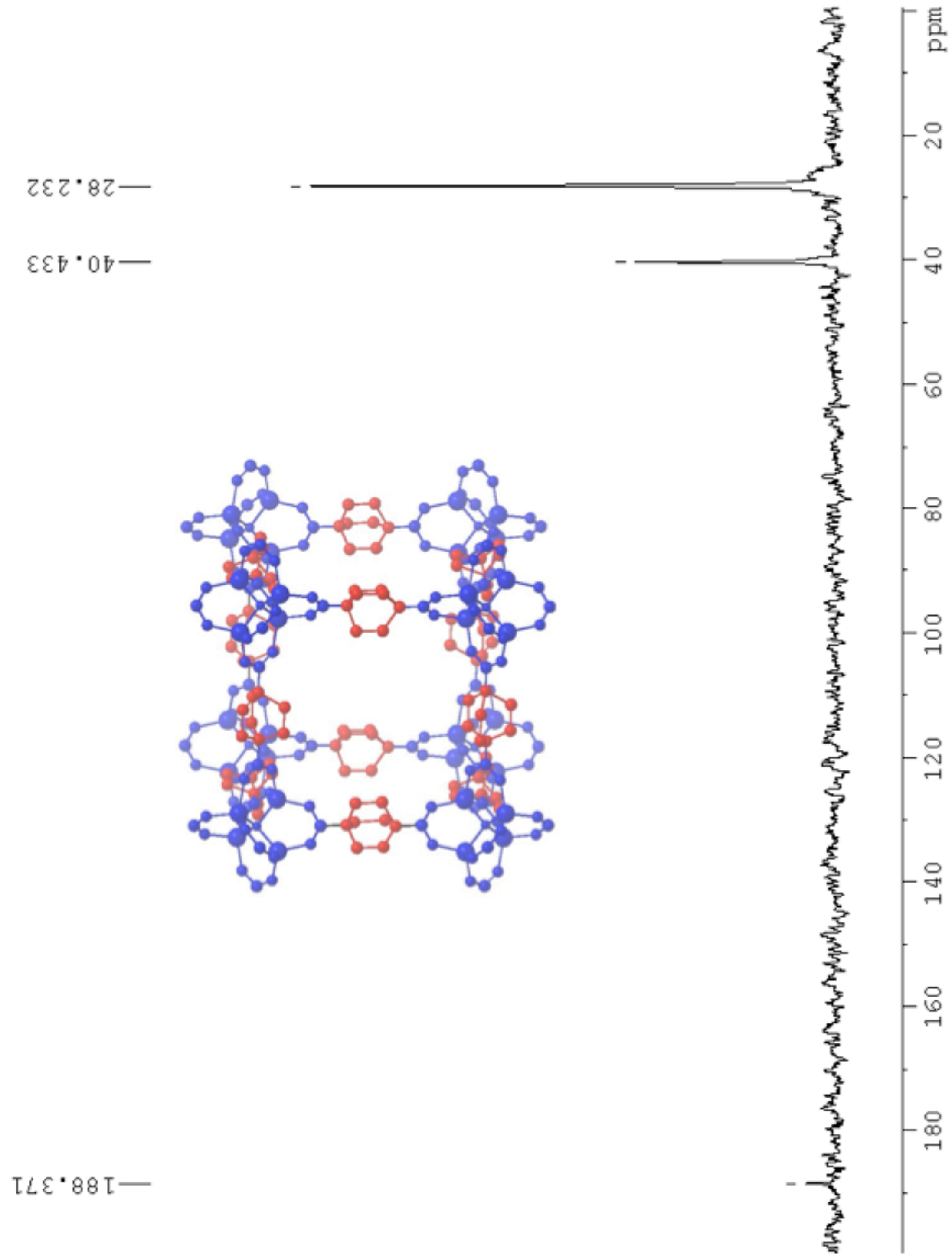

Figure SI-24. Activated BODCA MOF ^{13}C CP/MAS NMR spectrum, acquired by sandwiching between layers of anhydrous magnesium sulfate desiccant in the 4 mm rotor to prevent decomposition from ambient moisture. (MAS = 10 kHz, contact time = 4.4 microseconds, recycle delay = 20 s).

STUCTURAL SOLUTION OF BODCA MOF VIA POWDER X-RAY DIFFRACTION ANALYSIS

DATA COLLECTION

Powder X-ray diffraction data were collected using a Panalytical X'Pert Pro X-ray Powder Diffractometer θ-2θ diffractometer in reflectance Bragg-Brentano geometry employing Ni filtered CuKα lines focused radiation (1.54059 Å) at 1600 W (40 kV, 40 mA) power and equipped with a Na(Tl) scintillation detector fitted at 0.2 mm radiation entrance slit. Samples were mounted on zero background sample holders by dropping powders from a wide-blade spatula and then leveling the sample with a razor blade. The best counting statistics were achieved by collecting samples using a 0.02° 2θ step scan from 1 – 90° with an exposure time of 2 s per step. All measurements were performed at room temperature and atmospheric pressure.

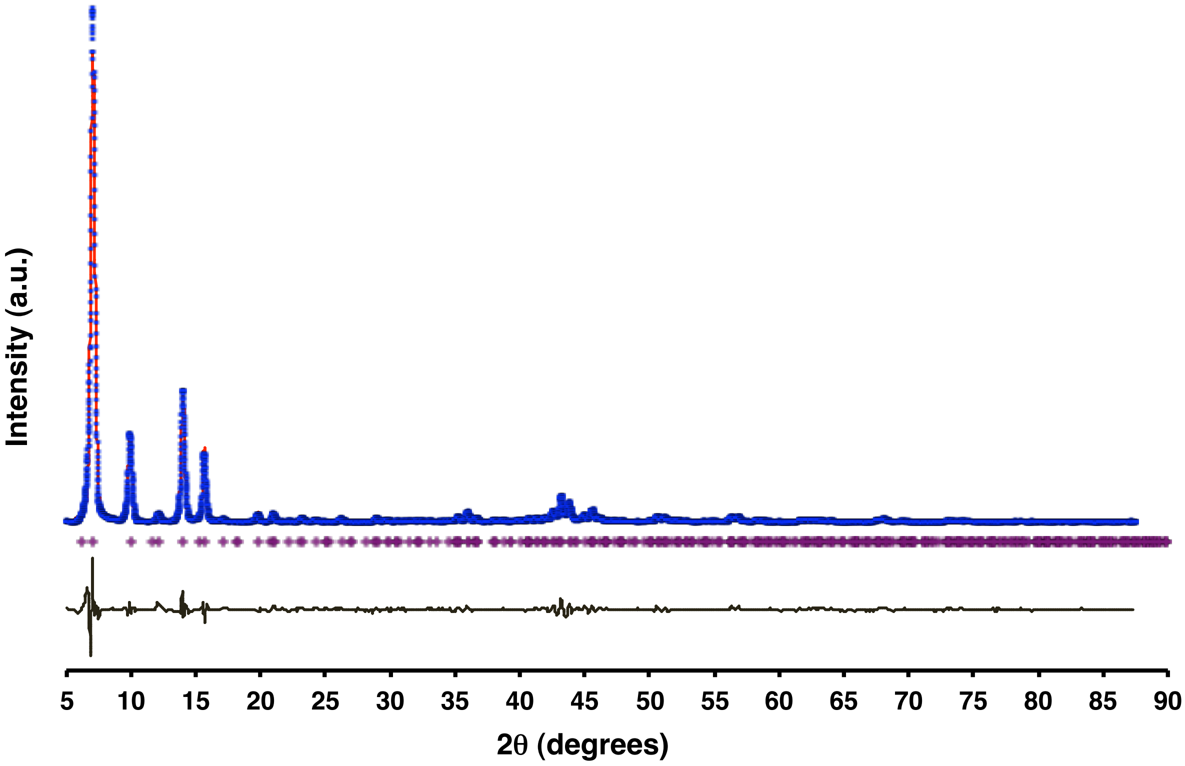

Figure SI-25. Experimental (blue ticks) and refined (red line) PXRD patterns of BODCA MOF after Rietveld refinement compared to the calculated pattern (black line) of the crystal model. The position of the Bragg reflections and the refinement difference plot are indicated as purple ticks and green line, respectively.

Unit Cell Determination

Unit cell determinations were carried out using Materials Studio[4] Reflex Indexing module for peak selection and interfacing with the TREOR. Satisfactory solutions in the cubic system were found with a_{TREOR} = 12.678(29) Å [Figures of merit $M(13)$ = 17, F_{13} = 11 (0.021722, 59)].

Pawley Refinements

Extraction of the integrated intensities (I_{obs}) were conducted by full-pattern-decomposition using the Pawley method in Topas[5] using data from 2θ = 5 – 80º. The background was first refined applying a 10nd order Chebyschev Polynomial. The profile was calculated starting with the unit cell parameters from the *TREOR* using $a' = 2 \cdot a_{\mathrm{TREOR}}$ (for a cubic supercell similar to MOF-5) and the space groups *P*23 and *P*1. The integrated intensities (I_{obs}) were extracted by a full pattern decomposition using a Thomson-Cox-Hasting pseudo Voigt peak profile, followed by refinement of peak asymmetry using Finger *et al.* asymmetry function. Unit cells and zero-shift were then refined with peak asymmetry. Once this was achieved, the background was refined with 20th-order polynomial. Refinement of unit cell parameters, zero shift, peak asymmetry, Lorentz polarization, crystallite size and strain, and linear absorption were used for the final profile. Residuals: R_{p} = 7.77, wR_{p} = 13.25, χ^2 = 4.04.

Electron Density Calculation

Electron density maps (Figure SI-26) were calculated using *SUPERFLIP* (Superflip—a computer program for the solution of crystal structures by charge flipping in arbitrary dimensions).[6] Calculations were made by adapting the powder pattern routine[7] with the histograms generated from a similar compound MOF-5[8] using the indexed integrated intensities obtained from the Pawley refinement. Electron density maps and their symmetry were also calculated using the space group *P*1 after equipartition of integrated intensities.

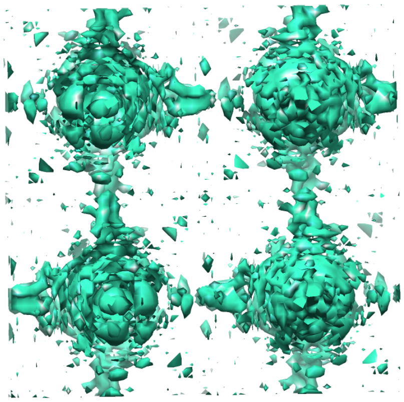

Figure SI-26. Example of a reconstructed electron density map obtained from *SUPERFLIP* (viewed along the 100 direction).

CRYSTAL STRUCTURE MODELING

The model for BODCA MOF, including cell parameters and atomic positions was generated using Materials Studio chemical structure-modeling software employing the Crystal Building module. The structure of BODCA MOF was first generated using the space group *Pm*-3, the cell parameters were used as obtained from LeBail refinement, and the atom positions were obtained from the MOF-5 structure by replacing the *p*-phenylene ring with 1,4-bicyclo[2.2.2]octane ring. The constructed structure was minimized with the Forcite module using the geometry optimization with the universal force field (UFF).[9] Further modeling for Rietveld refinements required increase of symmetry from *Pm*-3 to *Fm*-3*m* keeping unit cell constant and accounting for the fractional occupancy of the atoms due to the rapid rotation of the BODCA MOF bicyclo[2.2.2]octane rotators about their 1,4 axes.

Rietveld Refinements

Rietveld refinements were performed using GSAS (General Structure Analysis System),[10] using data from 2θ = 5 – 90º (Figure SI-25) up to a resolution of d_{min} = 1.16 Å. The profile used was GSAS function number 3, which consists on Thomson-Cox-Hasting modified pseudo-Voigt function with 6 terms, and Finger-Cox-Jephcoat peak asymmetry with 2 parameters, using peak cutoff of 0.007. The starting unit cell parameters and atomic positions were obtained from Materials Studio modeling, using space group Fm-3m. The background was initially hand fit to a 20th order Shifted Chebyschev polynomial. The profile was initially calculated using the model-biased LeBail full-pattern decomposition routine, refining first the Gaussian and then the Lorentzian components, followed by the asymmetry. Unit cell parameters, zero-shift corrections and Lorentz-polarization (LP) function were then refined observing convergent refinements. Following the LeBail fit, Rietveld routine with extraction of the structure factors (F_{obs}) was then used refining the scale factor, unit cell parameters, zero shift and LP function, followed by the background function and the crystallite size, strain broadening and anisotropic microstrain. Two oxygen atoms were included inside the pores (at 4*a* and 4*b* Wyckoff positions) to partially correct for the influence of water guest molecules (present from the interaction with ambient surroundings over the course of the PXRD data collection, as the TGA of the freshly activated BODCA MOF shows no mass loss until 450 °C), and their occupancy factors were refined with convergent results. A March-Dollase preferential orientation correction at the 100 plane was added to the refinements (after testing refinements with 100, 110, 111, 210 and 211 planes obtaining best fits with the 100 correction). Isotropic atomic displacement parameters (U_{iso}) of all non-hydrogen atoms were refined with constraints (constraining all the chemically equivalent atoms), in addition to the asymmetry function. U_{iso} of hydrogen atoms were then added with constraints and included in the refinements. During the course of the final refinements, the oxygen atom that accounts for guests at the 4*a* Wyckoff position constantly resulted in negative values of partial occupancy and thus was removed from the model. Final refinements included all before mentioned parameters with the exception of the profile parameters (32 parameters), which were refined with iteratively until convergent refinements were obtained. F_{obs} were extracted, bond distances and angles were calculated and a crystallographic information file (CIF) was generated.

Table SI-1. Crystallographic information from Rietveld Refinement.

Name	**BODCA-MOF**
Unit cell composition	$C_{420}H_{288}O_{106}Zn_{32}$
Unit cell mass formula (g mol^{-1})	6961.82
Assymetric unit composition	$C_{1.25}H_{1.50}O_{0.556}Zn_{0.167}$
Z	8
Crystal system	Cubic
Space Group	*Fm*-3*m* (No. 225)
a (Å)	25.5575(21)
V (Å^3)	16694(4)
Crystal density (g cm^{-3})	0.6923
Number of independent atoms	18
Observed reflections	732
Refined parameters (total)	49
Rp (%)	4.48
wRp (%)	7.30
R_B (%)	4.32
GOF (χ^2)	8.66

Table SI-2. Atomic Coordinates

Atom	*x*/*a*	*y*/*b*	*z*/*c*	Occupancy	U_{iso}
H1	0.8221	0.9533	0.3043	0.2500	0.5060
H2	0.7667	0.9529	0.1593	0.2500	0.5060
H3	0.6682	0.9530	0.2797	0.2500	0.5060
C4	0.4681	0.6933	0.7664	0.2500	0.1280
H5	0.4528	0.6815	0.8076	0.2500	0.5060
H6	0.4529	0.6622	0.7367	0.2500	0.5060
H7	0.5470	0.8347	0.7828	0.2500	0.5060
C8	0.8098	0.9684	0.2631	0.2500	0.1280
O9	0.2500	0.2500	0.2500	1.0000	0.1893
Zn10	0.2914	0.7086	0.2914	0.5000	0.1724
C11	0.7100	0.9686	0.2900	0.2500	0.1280
O12	0.2820	0.3600	0.7180	0.5000	0.1893
C13	0.5315	0.7930	0.7930	0.2500	0.1280
C14	0.6155	0.7500	0.7500	1.0000	0.1310
C15	0.2500	0.7500	0.5540	1.0000	0.2703
Zn16	0.2920	0.7920	0.7080	0.5000	0.1724
O17	0.7180	0.2180	0.3600	0.5000	0.2170
Ow2	0.5000	0.5000	0.5000	0.7047	0.0250

ASORPTION ISOTHERM DATA OF BODCA-D MOF

The dinitrogen adsorption isotherm (77 K) displays a sharp uptake with a single adsorption step at $p/p_o > 0.01$ followed by saturation, indicating a microporous material. It can be also described as a Type II isotherm under the IUPAC classification system (Figs. SI-27). Application of the Brunauer-Emmett-Teller (BET) model over $0.005 > p/p_o > 0.05$, according to the recommendation by Walton and Snurr.[11] resulted in a BET surface area of $S_{BET} = 2150$ m^2 g^{-1}. The total pore volume was determined from the Dubinin-Raduschevich (DR) model over the $0.13 > p/p_o > 0.35$ range, obtaining a $V_{p,DR} = 0.8630$ cm^3 g^{-1}. In the figure, the adsorption branch is represented by filled symbols and the desorption branch by open symbols, indicating the reversibility of the adsorption with no evident hysteresis.

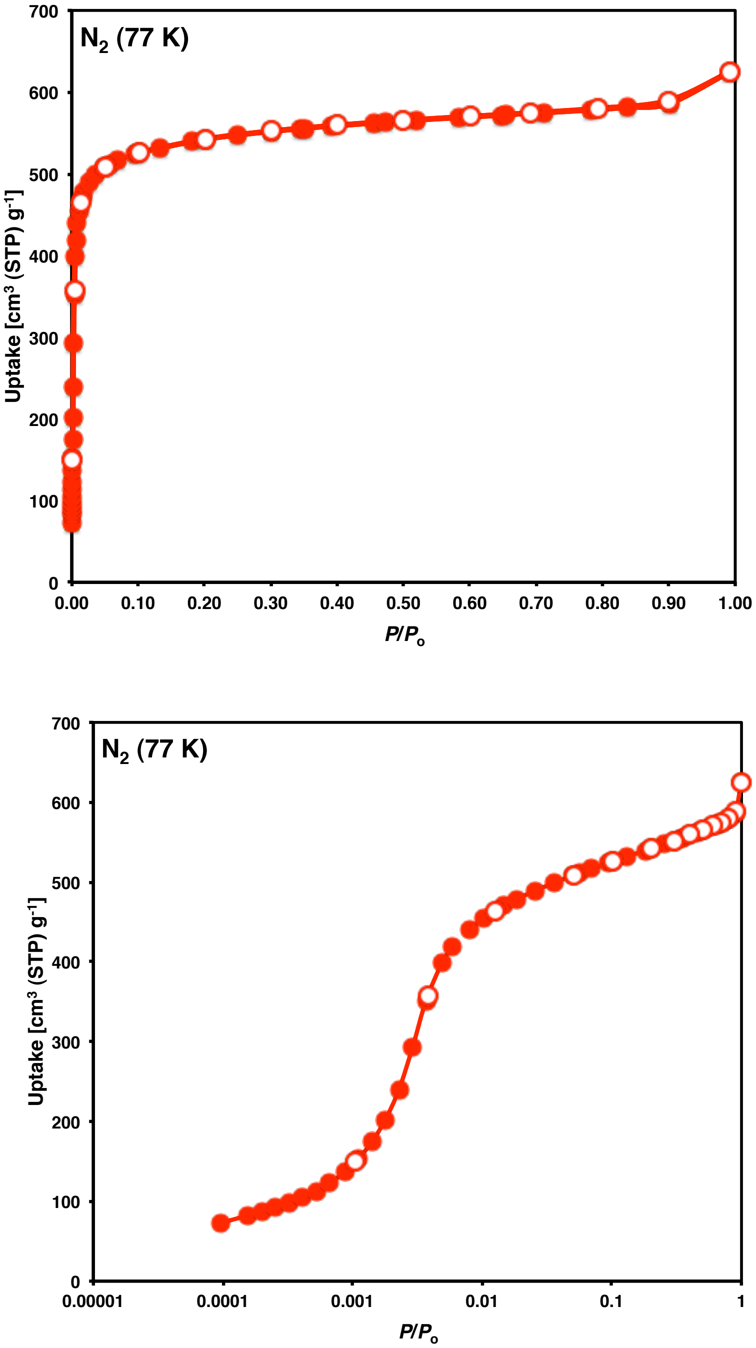

Figure SI-27. The dinitrogen adsorption isotherm (77 K) displays a sharp uptake with a single adsorption step at $p/p_o > 0.01$ followed by saturation, indicating a microporous material. It can be also described as a Type II isotherm under the IUPAC classification system. (a) Linear pressure scale. (b) Log pressure scale. In the figure, the adsorption branch is represented by filled symbols and the desorption branch by open symbols, indicating the reversibility of the adsorption with no evident hysteresis.

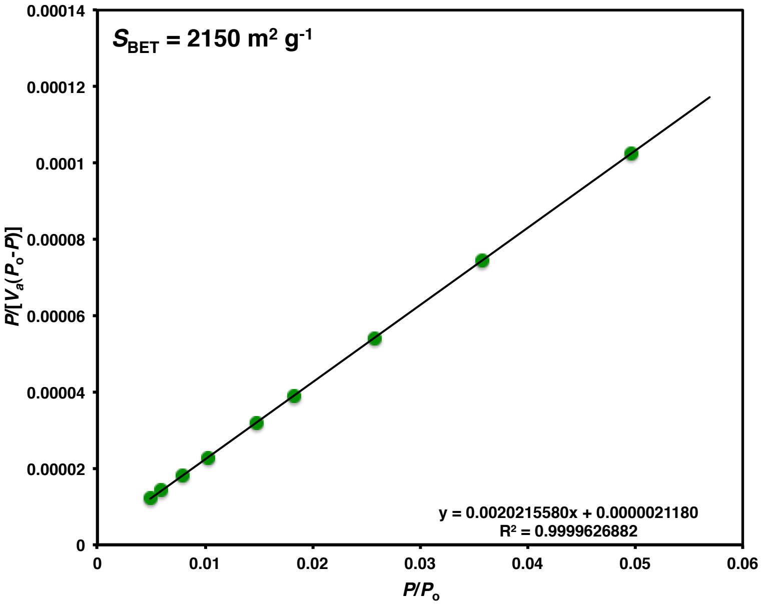

Figure SI-28. Application of the Brunauer-Emmett-Teller (BET) model over $0.005 > p/p_o > 0.05$, according to the recommendation by Snurr *et al.*[11] resulted in a BET surface area of $S_{BET} = 2150\ m^2\ g^{-1}$.

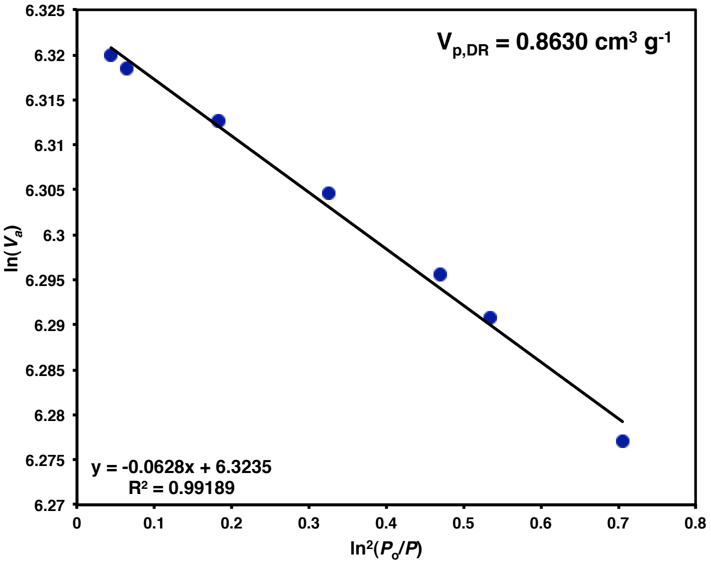

Figure SI-29. The total pore volume was determined from the Dubinin-Raduschevich (DR) model over the $0.13 > p/p_o > 0.35$ range, obtaining a $V_{p,DR} = 0.8630\ cm^3\ g^{-1}$.

SOLID-STATE NMR SPECTROSCOPY

^{13}C CP/MAS

The ^{13}C CP/MAS spectrum was acquired at UCLA using a Bruker DRX 300 spectrometer operating at a ^{13}C frequency of 75 MHz and a ^{1}H frequency of 300 MHz using a ^{1}H 90-degree ($\pi/2$) pulse width (*p*1) of 4.40 μs, a Hartmann-Hahn contact time of 5 ms, a data acquisition time of 66 ms, and a recycle delay of 20 s. The sample was sandwiched between anhydrous $MgSO_4$ dessicant in the 4 mm (outside diameter) rotor to prevent decomposition from ambient moisture over the course of the experiment, and was spun at a MAS rate of 10 kHz.

^{1}H SPIN-LATTICE RELAXATION

To determine the rotational dynamics and activation energy of the molecular rotors in BODCA MOF, proton spin-lattice relaxation (T_1) measurements were carried out at UCLA at two different ^{1}H Larmor frequencies of 29.49 MHz and 13.87 MHz and over a wide range of temperatures in the solid state. Wide-line ^{1}H spectra from 2.3 K - 80 K were measured in a polycrystalline BODCA MOF sample sealed in a capillary under an ultra-high purity helium atmosphere. A commercial electromagnet operating at a field strength B_o of 0.699 T or 0.322 T (for the high and low field measurements, respectively) was equipped with a solid-state NMR spectrometer and liquid helium cryoprobe built at UCLA. For the tank circuit, a very small NMR coil was constructed using PTFE-coated copper wire wound on a wire form. The capillary tube containing the polycrystalline BODCA MOF powder was inserted into the coil and held in place with a custom designed PTFE box. Acetone was used for cleaning the coil and its surroundings to reduce spurious proton signals relative to the BODCA MOF sample. The thermometer was calibrated by performing Cu T_1 measurements and correlating the relaxation times with the thermometer's resistance.

The ^{1}H spin-lattice relaxation was measured using a saturation recovery sequence combined with a spin-echo, in which a saturation pulse comb ($3 \times \pi/2$) was followed a time τ' later (τ' values taken from the variable delay list) with a π/2 pulse p_1 (typical pulse width $p_1 = 0.95$ μs) and subsequently a pulse p_2. The angle of p_2 is adjustable to maximize the spin-echo magnitude, and pulses were calibrated as necessary. Saturation recovery traces from 2.3 K to 80 K were fit well with a single exponential function (Figs. A.5.26. and A.5.29.).

If a given conformational motion or group rotation modulates a magnetic interaction (*e.g.*, dipolar coupling) and occurs at a rate that is near the Larmor frequency in an otherwise rigid lattice, the field that it generates may dominate the nuclear relaxation kinetics of the sample. If the process responsible for relaxation is thermally activated and follows an Arrhenius behavior with a correlation time τ_c (Eq. 5.2), the relaxation may be characterized as a function of temperature in order to elucidate its characteristic activation energy (E_a) and pre-exponential factor (τ_0^{-1}, or A). The fastest relaxation (shortest time) will occur when the rate of motion matches the Larmor frequency of the spins under observation in the corresponding magnetic field. For solid samples with strong spin dipolar coupling and rapidly exchanging groups undergoing rotation with a time constant τ_c, the temperature-dependence of the spin-lattice relaxation times at the Larmor frequency can be fit to the Kubo-Tomita relaxation expression (Eq. 5.3).[12]

$$\tau_c^{-1} = \tau_0^{-1} \exp(-E_a/RT) \qquad \text{(Eq. 5.2)}$$

$$^1\text{H } T_1^{-1} = C\,[\tau_c\,(1 + \omega_0^2\,\tau_c^2)^{-1} + 4\,\tau_c\,(1 + 4\,\omega_0^2\,\tau_c^2)^{-1}] \qquad \text{(Eq 5.3)}$$

The constant $C = (2/3)\,\gamma^2\,\mathbf{B}_{nuc}^2$ corresponds to dipolar interactions related to the relative positions of the nuclei that participate in the relaxation process. $\mathbf{B}_{nuc}$ is the static local effective dipolar field, and γ and ω_0 are the gyromagnetic ratio and the angular Larmor frequency, respectively, of the observed nucleus in a magnetic field. The corresponding ^{1}H NMR frequencies in our experiment (in units of $v_L = \omega_L/2\pi$) are 29.49 and 13.87 MHz.

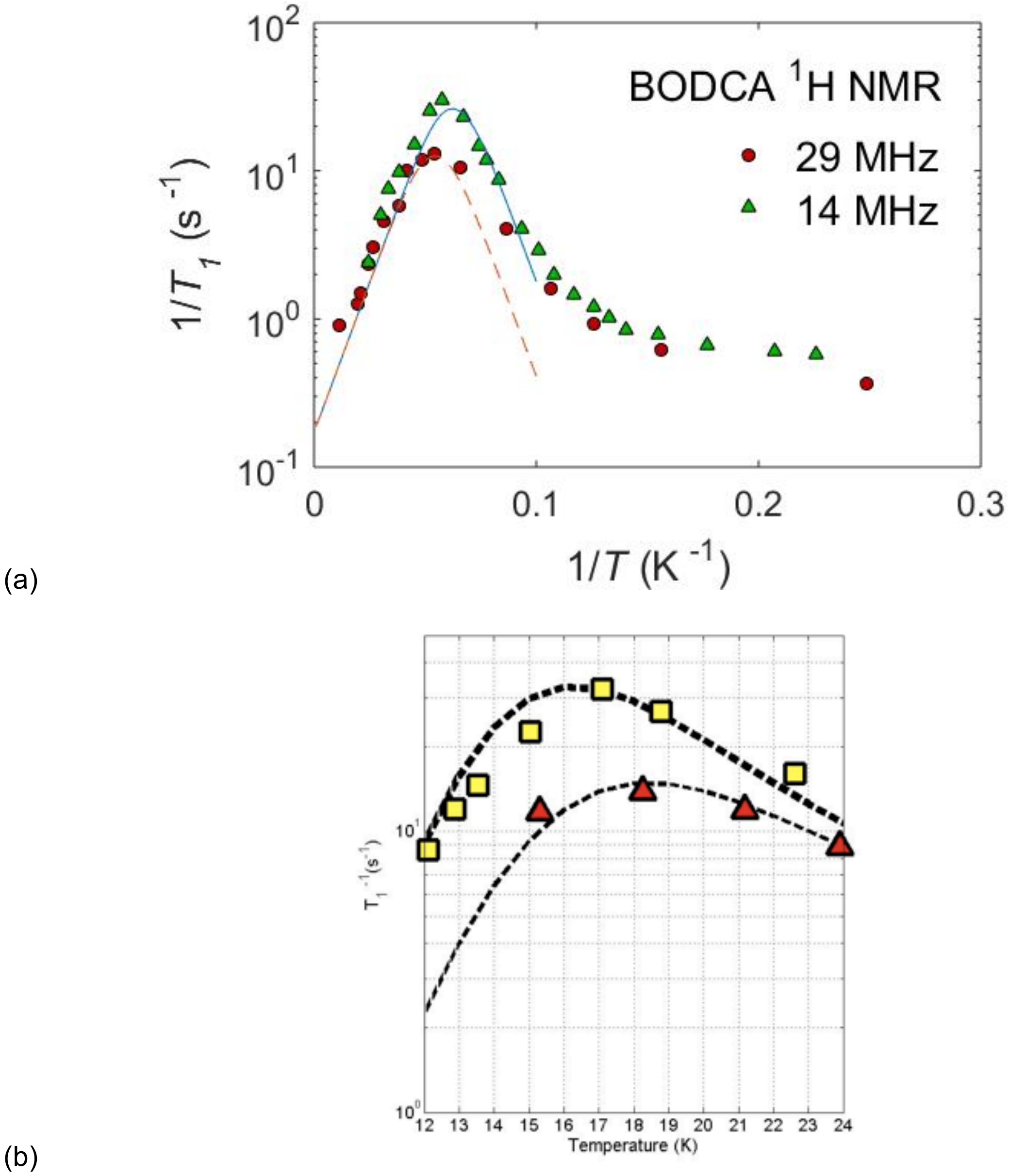

Figure SI-30. (a) Kubo-Tomita fit (black lines) to the ^1H T_1 relaxation data of the natural abundance BODCA MOF from T = 2.3 - 80 K, plotted with a semi-log scale for T_1^{-1} VS 1/T, where red corresponds to data collected at a Larmor frequency v_L= 29.49 MHz and yellow corresponds to v_L = 13.87 MHz. The high temperature data from both high and low field experiments can be fit well to the Kubo-Tomita fit, revealing an activation energy of only *ca.* 0.185 kcal mol^{-1} and a pre-exponential factor of 4.7 x 10^{10} Hz for both fits. (b) A zoom in of the data shows that the ^1H T_1 minimum occurs approximately 2.2 K lower at the lower field, in good agreement with the Kubo-Tomita fit for the same thermally activated process occurring at the two different Larmor frequencies.

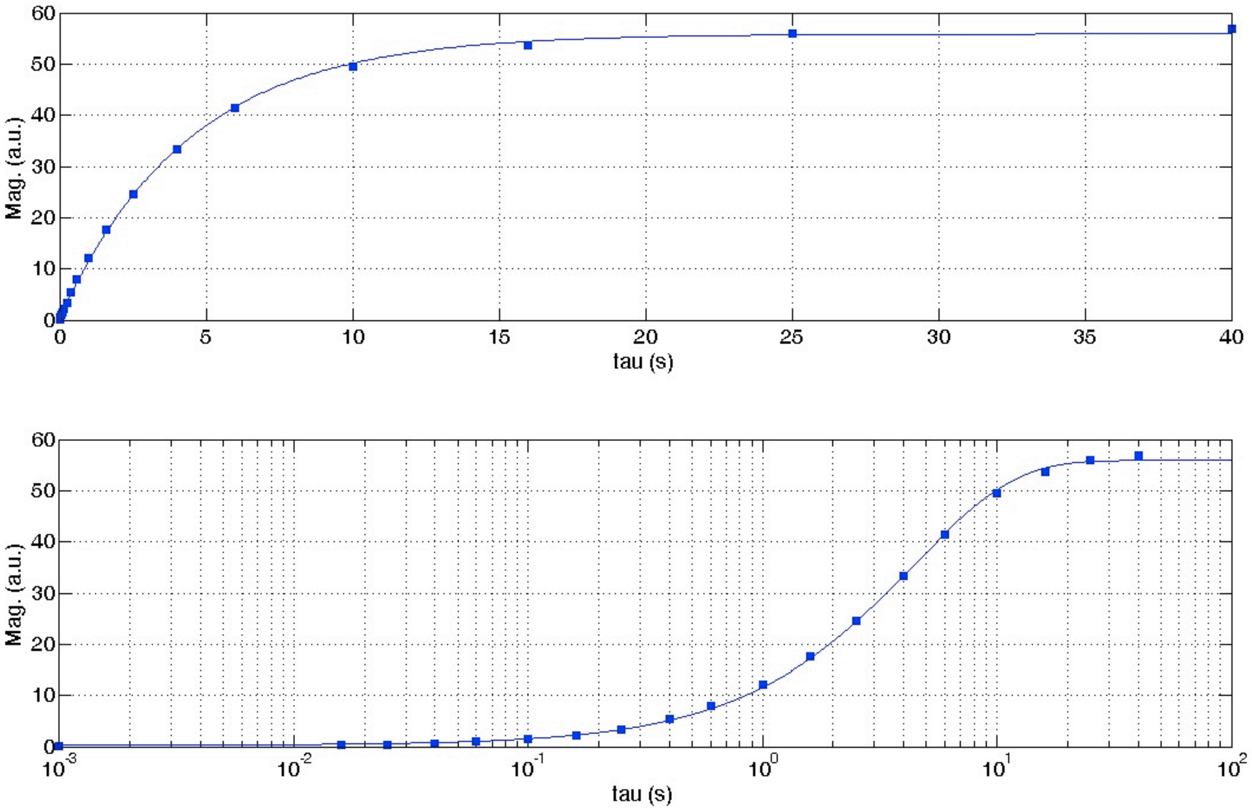

Figure SI-31. ^{1}H spin-lattice relaxation of the natural abundance BODCA MOF at 29.49 MHz, T= 2.3 K, fit to a single exponential.

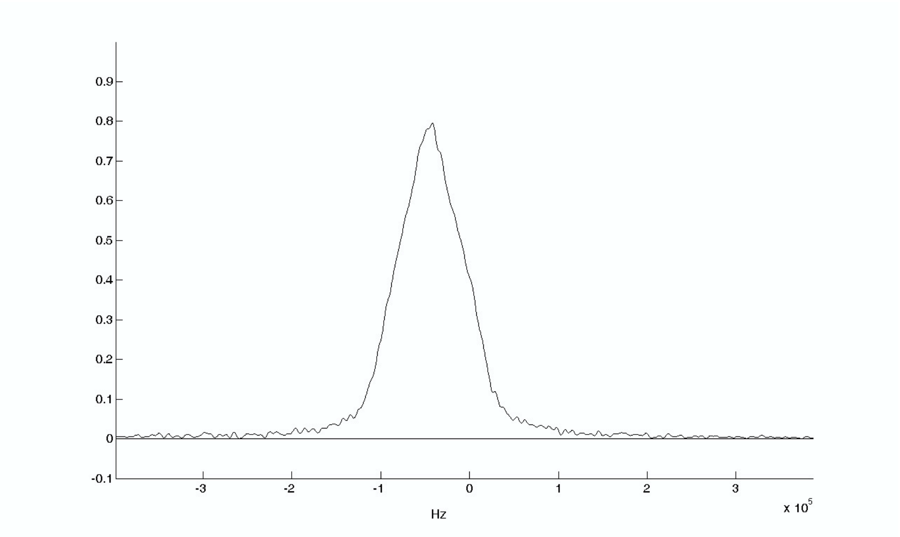

Figure SI-32. Fully recovered spectrum of natural abundance BODCA MOF, T = 2.3 K, of at a Larmor frequency of 29.49 MHz.

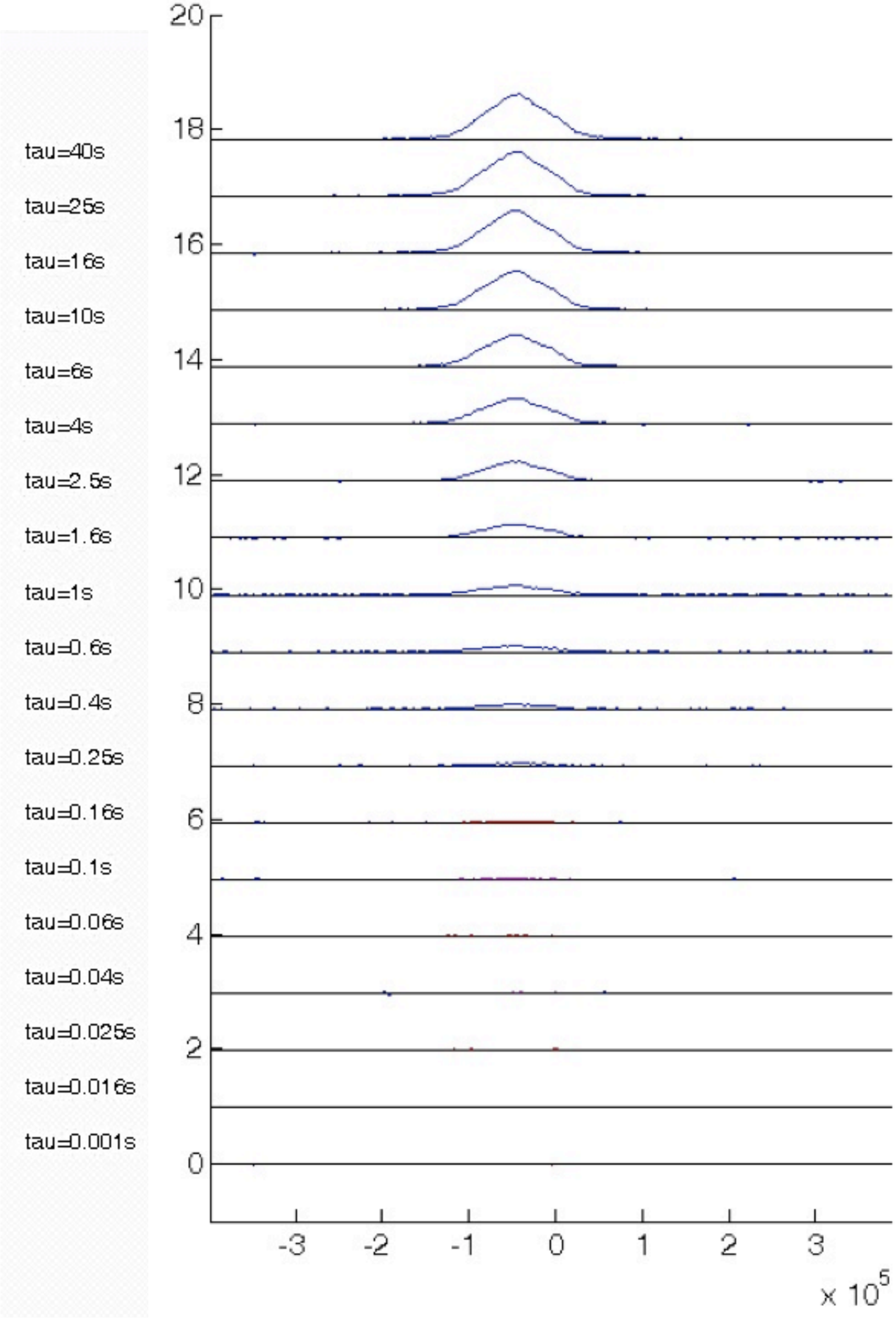

Figure SI-33. Stack plot of ^{1}H T$_1$ saturation recovery spectra according to the delay time tau (s) of the natural abundance BODCA MOF at 2.3 K and at a Larmor frequency of 29.49 MHz (*x*-axis in Hz).

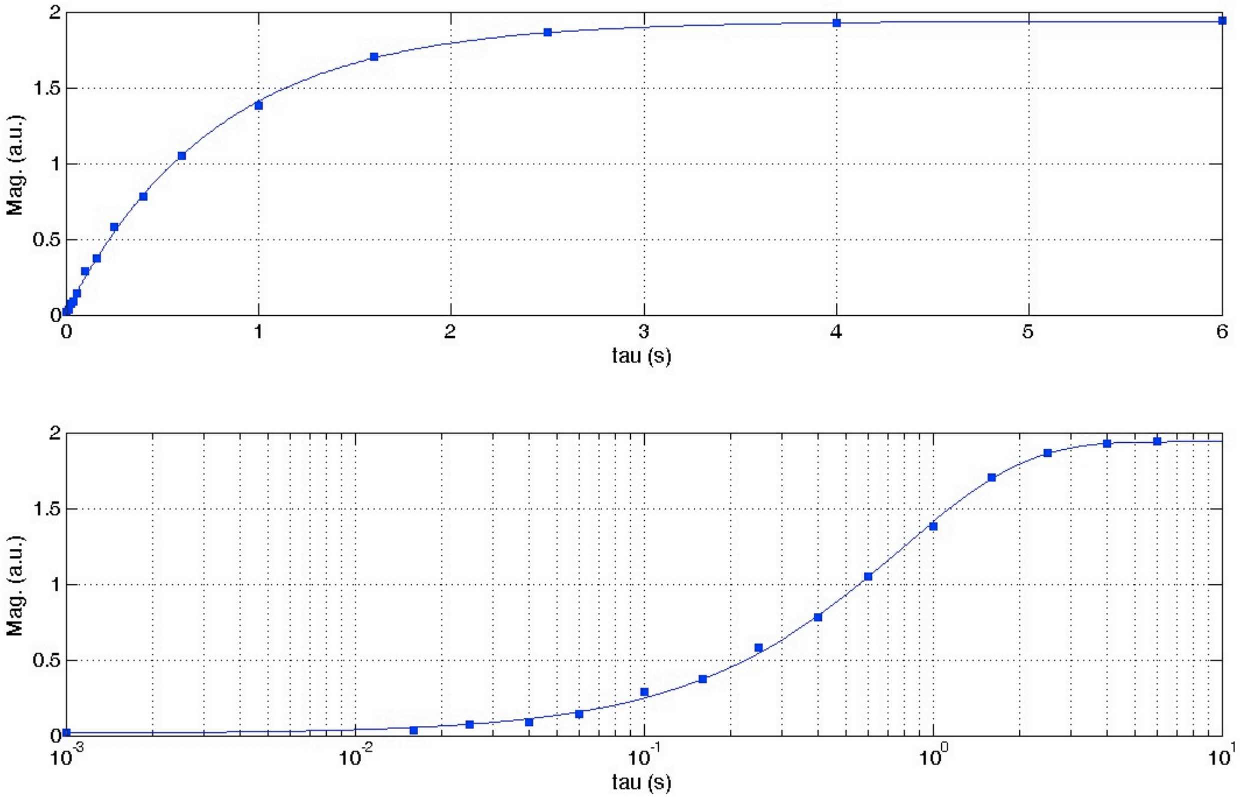

Figure SI-34. ^{1}H spin-lattice relaxation of the natural abundance BODCA MOF at 29.49 MHz, T = 49 K, fit to a single exponential.

^{2}H WIDELINE AND ZEEMAN SPIN-LATTICE RELAXATION

In order to determine a model of the 1,4-bicyclo[2.2.2]octane dynamics as it relates to its rotational potential, as well as to gain additional insight and complementary information about the dynamical activation energy and pre-exponential factor, ^{2}H solid-state NMR wide-line spectra and Zeeman spin-lattice relaxation times were acquired at Pacific Northwest National Laboratory's (PNNL) Environmental and Molecular Sciences High Field Magnetic Resonance Facility at a Larmor frequency of 76.78 MHz. A commercial superconducting Oxford magnet operating at a set field strength B_o of 11.7 T was equipped with a solid-state NMR spectrometer and 5 mm liquid helium cryoprobe built at PNNL. A saturation recovery sequence was employed to acquire periodically the ^{2}H spin-lattice relaxation times (T_1) as a function of temperature to enable selection of an appropriate recycle delay (Figure SI-34). Fully relaxed wide line spectra for line shape analysis were acquired with the quadrupolar spin-echo pulse sequence, $(\pi/2)x{-}t_1{-}(\pi/2)y{-}t_2$, with a typical $\pi/2$ pulse of 2.1 μs and a pulse spacing of $t_1 = t_2 =$ 50 μs. Theoretical simulation of the ^{2}H NMR wide line spectra for a three-site 120° jump model with large angle librations was performed by the program Express 1.0,[13] with a quadrupolar coupling constant of 170 kHz (determined from the 6 K spectrum in the slow-exchange limit, $k_{rot} \leq 1 \times 10^4$ Hz), a cone angle of 70 degrees, and an asymmetry parameter of $\eta = 0$.

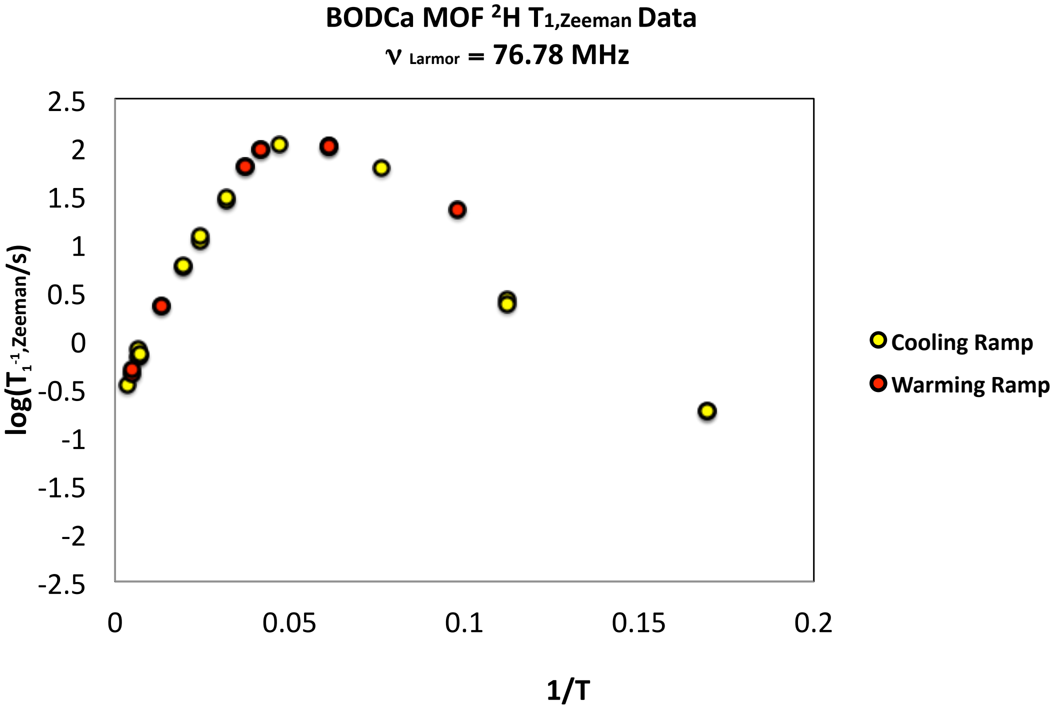

Figure SI-35. A saturation recovery sequence was employed to acquire periodically the ^{2}H spin-lattice relaxation times (T_1) as a function of temperature to enable selection of an appropriate recycle delay in the solid-echo experiments, shown with data corresponding to cooling and warming ramps in yellow and red, respectively. A minimum in relaxation time occurs at T ~ 21 K at a ^{2}H Larmor frequency of 76.78 MHz. This is consistent with the ^{1}H T_1 data, which shows a minimum in spin-lattice relaxation time at 18.2 K at a slightly lower Larmor frequency of 29.49 MHz, suggesting that the same motional process is being probed in each of the different experiments. At ~ 51 K and below, the ^{2}H spin-lattice relaxation deviates from single exponential behavior in agreement with the idea that at low temperatures, additional spin relaxation processes besides dynamical averaging may occur.

COMPUTATIONAL DETAILS

The rotational dynamics of the bicyclo[2.2.2]octane (BCO) unit in MOF crystal was studied using classical MD simulations and quantum mechanical (QM) calculations. Inspection of the MOF crystal structure indicates the rotation of a BCO group is not influenced by other BCOs or by the metal-organic frameworks. Consequently, we focused on calculations of independent 1,4-bicyclo[2.2.2]octane dicarboxylic acid (BODCA) molecules in the gas phase. We took coordinates of one BODCA molecule from the crystal structure and fixed the positions of the terminal carboxyl groups. Classical MD simulations were used to determine the details of the rotation of BCO fragments at different temperatures. QM calculations was used to compute the energetics of the rotational and the vibrational processes.

Classical MD simulations were carried out at 292 K and 41 K. The BODCA structure was first optimized w/ B3LYP density functional and the double-zeta 6-31G(d) basis set with constraints on the terminal carboxyl groups. Single point charges were computed with HF/6-31G(d) theory. All QM calculations were performed using G09 and the antechamber module in Amber12 to process atomic partial charges from the QM computations. Atomic partial charges were assigned with the RESP model, and the generalized Amber force field (GAFF) was used for further classical MD simulations. The BODCA structures were first optimized in the gas phase, and then heated to 41 K or 292 K for the MD simulations. The equilibration process was performed for 5 ns. Then MD trajectories were generated and collected for 10 ns at 292 K and 1 μs at 41 K. The dihedral angle of O-C_1-C_2-C_3 was plotted to show the rotation of BCO unit (Figure 1). For the 1 μs MD simulation at 41 K, no rotation was observed (frequency smaller than 1 MHz). At 292 K, rapid rotation was observed, with frequencies on the order of 1 GHz (more than 10 rotations observed in 10 ns).

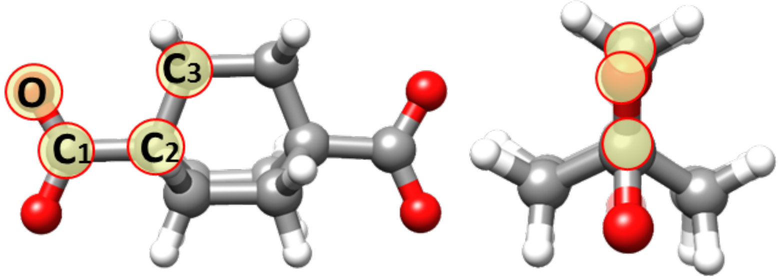

Figure SI-36. The optimized structure of BODCA, side view (left) and top view (right). Dihedral angle O-C-C-C (atoms circled in red) was used to represent the rotation.

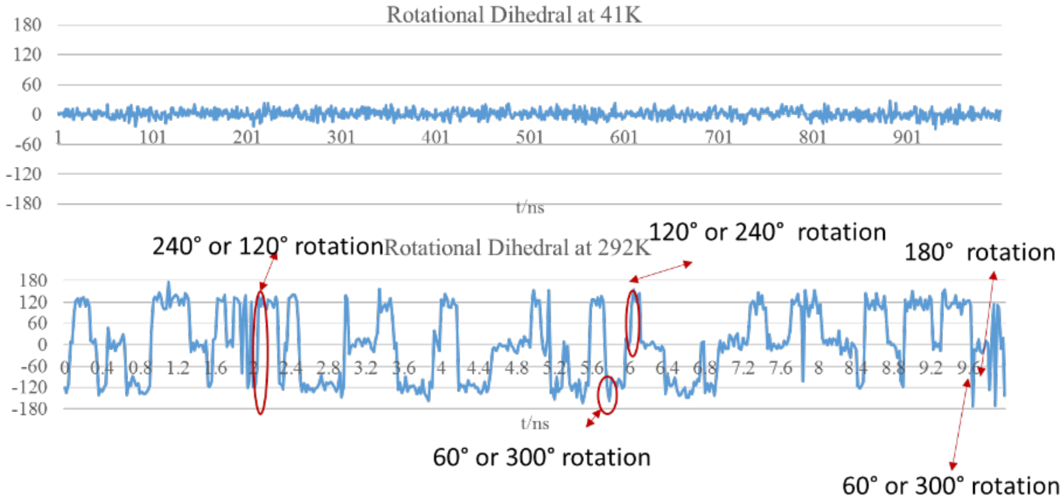
Rotational Dihedral at 41K

Rotational Dihedral at 292K

240° or 120° rotation

120° or 240° rotation

180° rotation

60° or 300° rotation

60° or 300° rotation

Figure SI-37. The dihedral angle changes in MD simulations.

Energy scans were done with various levels of theory and basis sets to test the energy barriers of the rotational process. We carried out QM calculations with the dihedral angle of O-C_1-C_2-C_3 constrained in the range of 0º to 180º at 5º increments. The energy plot from QM calculations shows that BCO group has a 6-fold rotation. The energy barrier for rotation given by each combination of methods and basis sets is below 1 kcal mol^{-1}. M062X/6-311+G(d) and ωB97XD/6-311+G(d) are more accurate compared to other methods and basis sets, and results with these two methods show that the energy barrier is only 0.1 kcal mol^{-1}, which is consistent with the experimental value of 0.185 kcal mol^{-1}.

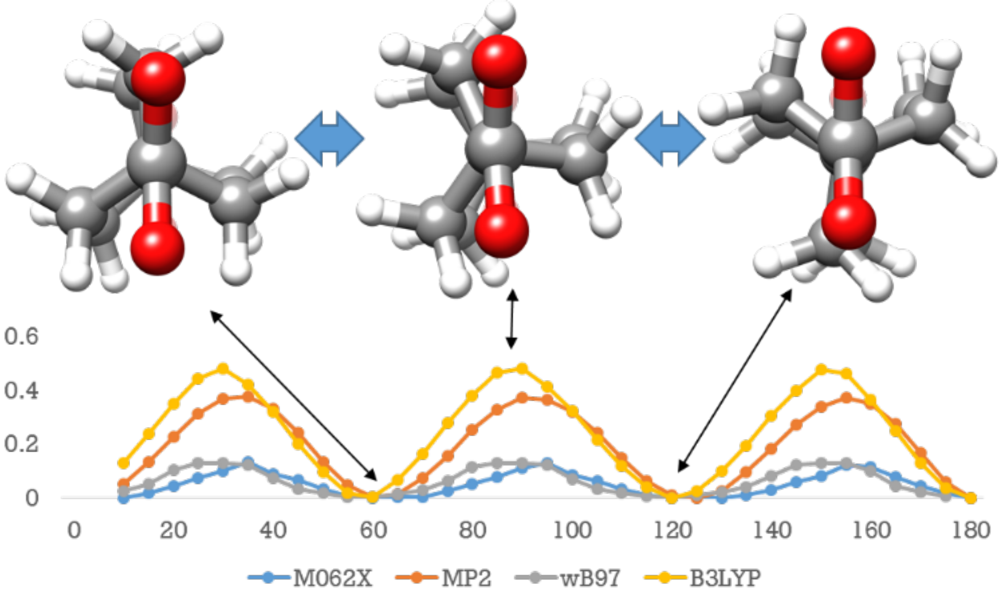

Figure SI-38. Energy scan of the rotational dihedral angle with four quantum mechanical methods [energy barriers]: Light blue dots, M062X/6-311+G(d) [0.1 kcal mol^{-1}]; orange dots, MP2/6-31G* [0.4 kcal mol^{-1}]; grey dots, wB97xd/6-311+G(d) [0.1 kcal mol^{-1}]; yellow dots, B3LYP/6-31G(d) [0.5 kcal mol^{-1}].

Besides the rotation of the BCO unit, there can be twisting vibrations of the BCO unit that can be observed experimentally. The twisting reduces the D_{3h} symmetry to D_3 symmetry of the BCO unit. We determined how various levels of DFT and Amber treat the twisting motion by scanning the dihedral angle $C_1C_2C_3C_4$ from -8° to 8° with a step size of 1° (figure 4). The D_{3h} structure has a dihedral angle of 0°. With MP2/6-31G(d) and B3LYP/6-31G(d), the D_{3h} conformation is the minimum (0.2 kcal mol^{-1} lower than D_3+ or D_3-). As calculated with M062X/6-311+G(d) and ωB97XD/6-311+G(d), D_3 conformation with dihedral angle of 9° is the minimum. The D_{3h} conformation is 0.2-0.4 kcal mol^{-1} higher than D_3+ or D_3- . The zero-point energy of vibration is 0.3 kcal mol^{-1} (corresponding to frequency of 113 cm^{-} calculated with ωB97XD/6-311+G(d)). The energy barrier observed with more accurate method/basis set (M062X/6-311+G(d), ωB97xd/6-311+G(d)) is very small, with the same range as the zero-point energy, we can conclude that BCO adapts a “quasi D_{3h} structure”.

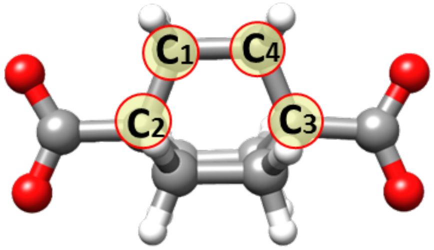

Figure SI-39. The dihedral angle C_1-C_2-C_3-C_4 (atom circled in red) were used to represent the vibration of BCO rotor.

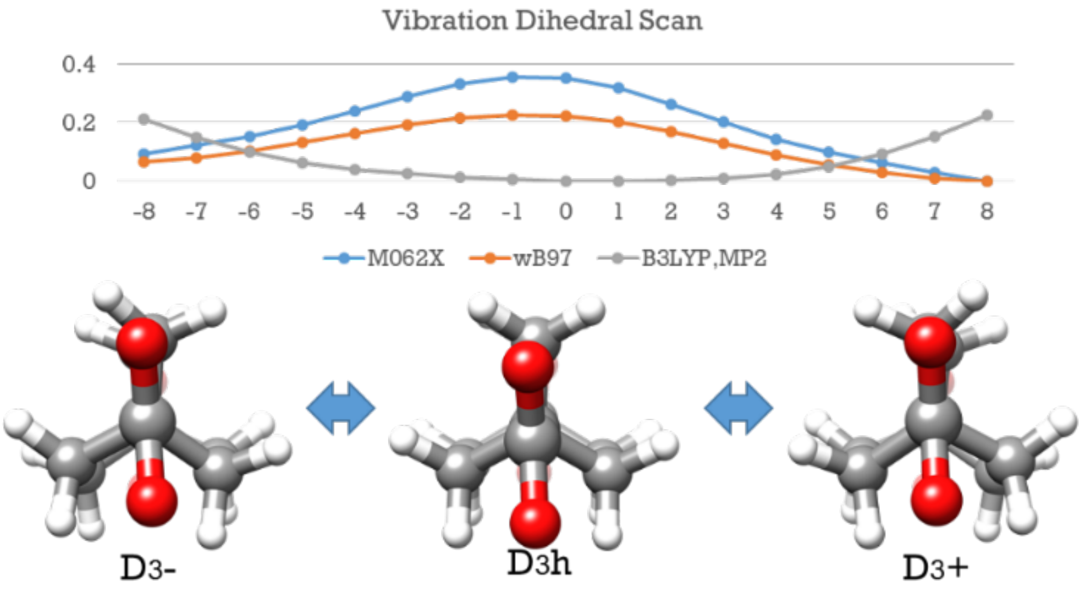

Figure SI-40. Energy scan of the vibrational process determined by four quantum mechanical methods indicating D_3 structures in a double well potential (energy maximum): Light blue dots, M062X/6-311+G(d) [0.4 kcal mol^{-1}]; orange dots, MP2/6-31G* [0.2 kcal mol^{-1}]. By contrast, the grey dots illustrating the results from the B3LYP/6-31G(d) method indicate a shallow energy minimum for the D_{3h} symmetric structure.

References

---

1 Karlen, S.D.; Reyes, H.; Taylor, R.E.; Khan, S.I.; Hawthorne, M.F.; Garcia-Garibay, M.A. Symmetry and dynamics of molecular rotors in amphidynamic molecular crystals*, Proc. Nat. Acad. Sci. USA* **2010**, *107*, 14973.

2 Holtz, H.D.; Stock, L.M. The Preparation of 1-carboxy-4-substituted bicyclo[2.2.2]octanes, *J. Am. Chem. Soc.* **1964**, *86*, 5183.

3 Majerski, Z.; Zuanic, M.; Metelko, B. Deuterium isotope effects on carbon-13 chemical shifts of protoadamantane, Evidence for geometrical dependence of 3.Δ. and 4.Δ. effects *J. Am. Chem. Soc*. **1985**, *107*, 1721.

4 Materials Studio v 5.0.0.0, 2009, Accelrys Software Inc.

---

5 DIFFRAC^{plus} Total Patterns Analysis Solution TOPAS 3.0 (Bruker AXS, Madison, WI, **2000**).

6 Palatinus, L.; Chapuis . G. *SUPERFLIP* – A computer program for the solution of crystal structures by charge flipping in arbitrary dimensions, *J. Appl. Cryst.* **2007**, *40*, 786.

7 Baerlocher, C.; McCusker, L.; Palatinus, L. Charge flipping combined with histogram matching to solve complex crystal structures from powder diffraction data, *Z. Kristallogr.* **2007**, *222*, 47.

8 CIF file of ZIF-8 was obtained from the Cambridge Structural Database with the reference code VELVOY. Park, K. S.; Ni, Z.; Côté, A. P.; Choi, J. Y.; Huang, R.D.; Uribe-Romo, F. J.; Chae, H. K.; O'Keeffe, M.; Yaghi, O. M. Exceptional chemical and thermal stability of zeolitic imidazolate frameworks, *Proc. Natl. Acad. Sci. USA* **2006**, *103*, 10186.

9 Rappe, A. K.; Casewit, C. J.; Colwell, K. S.; Goddard-III, W. A.; Skiff, W. M. UFF, A full periodic table force field for molecular mechanics and molecular dynamics simulations, *J. Am. Chem. Soc*. **1992,** *114,* 10024.

10 Larson, A. C.; VonDreele, R. B. General Structure Analysis System (GSAS) (Los Alamos National Laboratory Report LAUR 86-748, Los Alamos, NM, 2004)

11 Walton, K.S.; Snurr, R.Q. Applicability of the BET method for determining surface areas of microporous metal-organic frameworks, *J. Am. Chem. Soc.* **2007**, *129*, 8552.

12 (a) Kubo, R.; Tomita, A general theory of magnetic resonance absorption, K. *Phys. Soc. Jpn.* **1954**, *9*, 888. (b) Redfield, A.G. The theory of relaxation processes, *Adv. Magn. Reson.* **1965**, *1*, 1.

13 Vold, R. L.; Hoatson, G. L. *J.* Effects of jump dynamics on solid state nuclear magnetic resonance line shapes and spin relaxation times, *Magn. Reson.* **2009**, *198*, 57.